IN-SITU TEMPERATURE AND THICKNESS CHARACTERIZATION FOR SILICON WAFERS UNDERGOING THERMAL ANNEALING

A Thesis

by

VIKRAM VEDANTHAM

Submitted to the Office of Graduate Studies of
Texas A&M University
in partial fulfillment of the requirements for the degree of

MASTER OF SCIENCE

August 2003

Major Subject: Mechanical Engineering

IN-SITU TEMPERATURE AND THICKNESS CHARACTERIZATION FOR SILICON WAFERS UNDERGOING THERMAL ANNEALING

A Thesis

by

VIKRAM VEDANTHAM

Submitted to Texas A&M University
in partial fulfillment of the requirements
for the degree of

MASTER OF SCIENCE

Approved as to style and content by:

Chii-Der S. Suh (Chair of Committee)	Ravinder Chona (Member)
Andrew Chan (Member)	Dennis L. O'Neal (Interim Head of Department)

August 2003

Major Subject: Mechanical Engineering

ABSTRACT

In-Situ Temperature and Thickness Characterization for Silicon Wafers

Undergoing Thermal Annealing. (August 2003)

Vikram Vedantham, B.E., Annamalai University, India

Chair of Advisory Committee: Dr. Chii-Der S. Suh

Nano scale processing of IC chips has become the prime production technique as the microelectronic industry aims towards scaling down product dimensions while increasing accuracy and performance. Accurate control of temperature and a good monitoring mechanism for thickness of the deposition layers during epitaxial growth are critical parameters influencing a good yield. The two-fold objective of this thesis is to establish the feasibility of an alternative to the current pyrometric and ellipsometric techniques to simultaneously measure temperature and thickness during wafer processing. TAP-NDE is a non-contact, non-invasive, laser-based ultrasound technique that is employed in this study to contemporarily profile the thermal and spatial characteristics of the wafer. The Gabor wavelet transform allows the wave dispersion to be unraveled and the group velocity of individual frequency components to be extracted from the experimentally acquired time waveform. The thesis illustrates the formulation of a theoretical model that is used to identify the frequencies sensitive to temperature and thickness changes. The group velocity of the corresponding frequency components is determined and their corresponding changes with respect to temperature for different thickness are analytically modeled. TAP-NDE is then used to perform an experimental analysis on Silicon wafers of different thickness to determine the maximum possible resolution of TAP-NDE towards temperature sensitivity, and to demonstrate the ability to differentiate between wafers of

different deposition layer thickness at temperatures up to 600ºC. Temperature resolution is demonstrated for ±10ºC resolution and for ±5ºC resolution; while thickness differentiation is carried out with wafers carrying 4000Å and 8000Å of aluminum deposition layer. The experimental group velocities of a set of selected frequency components extracted using the Gabor Wavelet time-frequency analysis as compared to their corresponding theoretical group velocities show satisfactory agreement. As a result of this work, it is seen that TAP-NDE is a suitable tool to identify and characterize thickness and temperature changes simultaneously during thermal annealing that can replace the current need for separate characterization of these two important parameters in semiconductor manufacturing.

ACKNOWLEDGEMENTS

The successful completion of this study has been highlighted by a huge contribution from a variety of people, each of whom played an equally important role in the establishment of the physical content of this work, and also in imparting the much needed encouragement and support.

I wish to thank Dr. Steve Suh for his immense contribution towards this study. His academic support in terms of knowledge, advice and equipment, and an ever-welcome attitude towards attending to problems makes him invaluable to this thesis work. As a knowledgeable person, a good critic, and a source of inspiration, he has been a guiding light in this endeavor.

I also wish to thank Dr. Ravinder Chona for his constant persistence upon tending to newer ideas and methods, and for his support in this project. A good-natured person, well versed with the nuances of design and mechanics, he has been a source of valuable information for the materialization of this project work.

I am also grateful to Dr. Andrew Chan of the department of Electrical Engineering, TAMU, for his help in resolving signal processing issues that are fundamental to this research.

In the course of this work, the hands of many have influenced the final outcome of the research. I wish to thank my research group members at the Photomechanics Laboratory, who, during the past two years of research, have solved and explained my endless questions and doubts, and have helped me with every step of experimentation.

A special word of gratitude is due to Randy Tucker, a source of immense knowledge and ideas towards design for experimentation. As a hands-on person to guide me towards the

realization of the experimental setup, and also as a true friend to share ideas with, his support and contribution towards this work is immeasurable.

As a last word, I am grateful to my family and friends all of whom are the inspiration to get to where I am right now. It is with their dedication and endless prayers and blessings that I was propelled towards the successful completion of this research.

My work is never complete without the blessings of God in all that I have achieved, and what I will in the future. He is Supreme, and in Him is everything.

TABLE OF CONTENTS

Page

CHAPTER Page

LIST OF FIGURES

FIGURE Page

LIST OF TABLES

CHAPTER I

INTRODUCTION

The semiconductor industry has witnessed the progress of fabrication of IC chips over the past half a century. Semiconductor device fabrication has been rightly dubbed as the science of miniaturization, with structural dimensions stepping down from the sub-millimeter scale to the sub-micron, and even the nano-scale.

Silicon was found to be the ideal raw material for electronics because of its dominant properties like high stability during thermal processing, effective thermal oxide formation, availability, and low defect densities. Until 1959, all electric components were discrete and similar, and had to be wired together to form functional circuits. In 1959, Robert Noyce [1] demonstrated the process of diffusion of various layers onto a substrate of silicon to make a transistor, leaving a thermal oxide protection on the junctions. Jack Kilby [1] of Texas Instruments solved the problem of wiring, by making silicon as a single capacitor on which all components can be fabricated. This integration helped component connections to be interlaid on the silicon substrate.

This formed the basis of the existing electronic and microelectronic devices in the world today. Transistors were able to address issues of rapid switching that are the central units of the state of the art electronic devices of this generation. Device miniaturization helped to reduce space, energy and has helped in the design of faster electronic units.

Along with this development came the need to carry out IC unit fabrications on the silicon wafer, and also complex assembly and circuit design. Decrease in product dimensions

---

This thesis follows the style and format of Ultrasonics journal.

necessitated research to recognize progressive techniques of chip manufacture, so that qualitative (performance) and quantitative (mass production) results are simultaneously achieved.

Early techniques of dopant introduction into the lattice involved ion implantation, where dopant ions were accelerated through an electrostatic field towards the solid surface. Penetration depth could be regulated to some extent by controlling the ion current. During the process of annealing at high temperatures, redistribution of dopant atoms resulted in undesirable properties. Implant damages could not be annealed unless the wafer is subjected to high temperature treatment.

Standard surface annealing techniques create short term annealing effects across the wafer, causing temperature gradients and significant diffusion. Moreover, large batch processing of wafers result in more non-uniformity, and is a compromise on quality.

The study presented in the thesis volume involves a quantitative non-destructive examination of Rapid Thermal Processing (RTP) in semiconductor production. RTP was introduced as a technique for implant annealing, but spread to other processing stages like vapor deposition and thin film growth. Layer growth on the silicon substrate is performed at elevated temperatures. This process is called Epitaxial growth, where patterned dopant regions are generated below the wafer surface. Single crystal layer growth of the order of sub-microns requires precise monitoring systems to ensure desired properties of the semiconductor device.

RTP is a single wafer processing system that reaches high temperatures in a very short interval of time and provides best uniformity and repeatability. With applications extending to epitaxial growth, the primary concern has been to ensure uniform thickness and temperature across the wafer. The processing time in the thermal chamber is of the order of a few seconds, during which temperature ramps to as high as 1100ºC. Non-uniform coatings across the wafer result in changes in localized electrical conduction properties that severely hamper the desired

performance of the circuitry. Minor fluctuations in temperature can cause localized heating and cooling zones across the wafer, which result in non-uniform coatings, warping and in severe cases, cause wafer breakage.

Wafer thickness is thus a fundamental issue addressed in RTP systems. Most of the existing thickness measurement techniques are post-processing methods, where repeatability issues cannot be accommodated due to varying RTP conditions from one run to another. One of the earliest methods of measuring thickness was the use of sheet resistance to understand film growth. Sheet resistance study used the Van der Pauw method to determine resistivity of the semiconductor. A four-point probe measured current-voltage characteristics across alternating pins after wafer processing, from which sheet resistivity could be determined.

Another ex-situ process termed surface profilometry involved exploration of different techniques from stylus measurement to optical methods to create a surface profile. Stylus profilometry involved the recording of the vertical displacement of a mechanical-transducer type probe called a stylus. The stylus was a point probe, and was dragged across the surface a number of times till the whole surface was adequately covered. This set limits on lateral resolution, and was limited by the probe tip dimensions. Also, multiple scans were necessary, and the damage caused by the tip of the stylus had to be accounted for.

Early temperature monitoring mechanisms involved the initial use of thermocouples as contact probes on the wafer surface. This caused localized impedance and resulted in cool zones on the wafer, which had a severe impact on thin film growth. Pyrometry was a solution that studied emissivity on one side of the wafer to map temperature profiles. However, this technique has limiting criteria such as upper temperature limit, the effective emissivity due to polysilicon and oxide layers, and window thickness determination.

Early examination of alternatives for conventional pyrometry was the use of different semiconductor processes to help calibrate the thermal properties of an RTP system. Hodul et al [2] explored dopant activation and sintering of refractory silicides to determine temperature uniformities and RTP equipment performance by studying thickness variations. Sheet resistance patterns indicated that film non-uniformities affect temperature uniformity. However, sheet resistance uniformity of the as-deposited film is a function of both film thickness and stoichiometric composition of the deposited film. Variations in oxygen content, for example, would show variations in sheet resistance for uniform film thickness.

Ellipsometric techniques were established on these lines where light of a constant wavelength was monitored for interferometric patterns. The resulting patterns were observed using a CCD camera for capturing fringe patterns. Ellipsometric analysis was found to be a suitable alternative to sheet resistance measurements of thickness, as this would be insensitive to stoichiometric variations.

Optical profilometry techniques offer better resolution, whole-field study, faster processing times, and non-destructive evaluation. Processes like speckle profilometry, white-light technique and phase shifting interferometry techniques use scanning interference microscopes and Michelson interferometers to study out-of-plane displacements.

Asinovsky et al [3] studied the progress of TiN films using ellipsometry with multiple angles of incidence at the 458 nm wavelength. This method was proven to work in accordance with results from profilometry, and showed the wafer to be center thick, while sheet resistance showed it to be center thin. However, ellipsometry involves modeling of reference optical constants used to measure thickness. Upon unavailability of these constants, parametric representations are generated. The authors used a harmonic oscillator representation, where each layer thickness was approximated by a parameter. Moreover, sensitivity of the technique is a

measure of the thickness of the film. The penetration depth of the light limited accuracy and ability to measure using ellipsometry. Typically, there is zero sensitivity above 600Å for 632 nm wavelength, and above 1400Å for 458 nm blue wavelength.

RTP evaluation based on measurements of oxide thickness was an alternative suggestion by Zollner et al [4] to help determine the temperature profile using semiconductor processes. The thermal cycle time for oxidation was shown to play an important role in determining oxide thickness. Wafers with different process times were studied using an ellipsometer after oxidation, and the corresponding oxide film thickness was determined. Temperature overshooting near the edges during initial heat-up was found to cause oxide layer inhomogeneities and extra growth at the boundaries of the wafer.

A quantitative evaluation tool is thus required to accurately map thickness uniformity across the wafer over the working temperature range. The tool must be sensitive to detect thickness variations over different temperature zones to the desired accuracy level of ±1ºC, so that it can precisely determine the uniformity of the deposited film. Moreover, it would be of utmost value if the tool can monitor both temperature and thickness changes simultaneously to the desired level of accuracy. The technique should have minimal to zero interference with the working conditions, and should be repeatable and reliable.

The use of acoustic waves in this aspect has sparked possibilities of achieving the desired resolution in these parameters. Lamb was the first to introduce the generation and propagation of elastic waves through plate-like structures. Homogeneous lamb wave equations for an elastic wave propagating in an isotropic plate was presented. The velocities of the symmetric (S_o) and anti-symmetric (A_o) modes were found to be the plate wave solutions. The dispersive characteristics of these waves that travel at different velocities were shown to be

useful to determine mechanical properties. However, in this study, a different set of conditions for elastic wave propagation would be used because of the anisotropic nature of silicon.

In theory, Lamb waves are known to have infinitely many modes characterized by the symmetric and anti-symmetric displacements about the central plane of the plate. However, the most sensitive segments of these modes to wave propagation in silicon needs to be located and studied to identify thickness variations. The process of identification of these sensitive frequencies, and their corresponding group velocities has to be analytically modeled in order to understand the behavior of these waves. This would serve as a source of prediction and validation during laboratory runs of test methods. The work presented here would help set the guidelines for creating a three-dimensional model to elaborate on thickness variations on temperature with group velocity as the governing function to study propagating guided waves in silicon.

Hutchins et al [5] investigated laser-generated ultrasound using a Q-switched Nd:YAG laser. Thermal expansion created strains in the metal at the point of generation, which act as the source of the acoustic pulses. The efficiency of generation, effects of ablation, and the modification to longitudinal directivity patterns were accounted for.

Traditional transducer based techniques for triggering and capturing Lamb waves on surfaces are good for identified frequency bandwidths. However, the bandwidth becomes a restriction on studying other modes of the generated dispersive waves. In a comparative study of transducer based sensing and interferometry, Dewhurst et al [6] demonstrated the effectiveness of a laser interferometer for data collection from a propagating wave generated by a pulsed Nd:YAG laser. Laser based ultrasonic characterization has been chosen to quantify Lamb wave behavior in this thesis, because of their non-contact nature, and broadband sensing and generation capabilities.

Kishimoto et al [7] examined the applicability of the wavelet transform to study the dispersive nature of structural waves. The Gabor wavelet was shown to be effective in decomposing the strain response of the system into its time-frequency components. Wave arrival times were identified, that helped determine the group velocity for the whole range of frequencies. Using Gabor Wavelet Transform (GWT) as the analyzing parameter, the waveform from silicon would be characterized for simultaneous thickness and temperature study.

The application of thin films in recent times has led researchers to try thickness and elastic property estimation of such layers deposited on different substrates. Hayashi et al [8] attempted a quantitative analysis of velocity dispersion of Lamb waves on metallic foils to estimate material properties. Group velocity dispersion of the A_o mode was studied using wavelet transformation, which agreed with the numerical solutions from the Rayleigh-Lamb equation.

Hurley et al [9] used laser ultrasonic methods for thin film property measurements by generating high frequency surface acoustic waves (SAW) waves for a series of TiN film samples on steel and Silicon. Laser based generation and sensing was used and dispersion curves indicated that at a given frequency, SAW velocity increased with increasing thickness. Attempts were made at correlating the dispersion relations to determination of elastic moduli of the specimen.

The presence of multi-layered films on substrates was studied theoretically by Grimsditch [10] to determine the elastic constants for anisotropic superlattices. Relations for the nine independent elastic constants for the lattice with orthorhombic symmetry were formulated that help in estimating the effective elastic moduli of the combined layers.

Habeger et. al [11] determined the dispersive wave relations for ultrasonic plate waves by studying its propagation on machine-made paper. The paper was modeled as an orthotropic

plate, and the wave vector in the z-direction was calculated using the stress-strain relations. The orthotropic plate wave dispersion equation was obtained by applying the boundary conditions to the possible plate wave solutions. Dispersion curves could be generated for symmetric and anti-symmetric modes of wave propagation. These relations will be shown to be the basis for the analytical model generated in Chapter II.

Schneider et al [12] investigated the applicability of a laser-acoustic method to examine properties of multiple layers with cubic crystal lattice. Layers of diamond-like carbon and aluminum were coated on steel and [100] silicon, and sensing was done using a piezoelectric transducer. Dispersion relations showed that multiple layers reduced the effective elastic moduli of the system, and thus the wave travels slower for a fixed frequency.

This thesis is a feasibility study of an alternative technique called Thermo-Acousto-Photonic Non-Destructive Evaluation (TAP-NDE), consisting of a pulsed Nd: YAG and a Fiber-Tip-Interferometer (FTI) setup that was developed at Texas A&M University. The two-fold objective of this thesis study is

- To experimentally establish the feasibility of TAP-NDE towards achieving a resolution of up to ±1ºC, which is the current requirement of the semiconductor industry, and
- To experimentally determine if TAP-NDE is capable of differentiating between a plain wafer, and a wafer of known deposition layer thickness.

Laser induced stress wave thermometry during actual silicon wafer processing, using TAP-NDE has been explored extensively by Rabroker [13]. A thermo-mechanical model for a wafer of constant thickness was developed on the grounds of dispersive plate-wave relations shown by Habeger et al [11], and elastic constants were simulated to vary with temperature and group velocity was shown to be a function of temperature. The experimental results were

generated using TAP-NDE for a temperature range of 40ºC to 400ºC, with a ±20ºC resolution. The resulting group velocity plots were shown to be in agreement with the theoretical model.

In the present study, temperature resolution of up to ±1ºC would be achieved by designing a closed thermal chamber system, so as remove the convection effects that were present in the previous experimental setup. This would also help in reaching higher temperatures, so that the simulation is closer to commercial wafer processing units.

Analytical modeling would be done on the principles of determination of elastic moduli as shown by Grimsditch [10]. However, changes in crystal lattice would be accounted for, by considering a titanium layer as the bonding layer between aluminum/copper and silicon, and a more general model for better applicability would be generated. The model would use effective elastic constants derived for the different deposition layer configurations. Using the experimental setup, the change in group velocity of a particular frequency for a plain Silicon substrate, and a wafer of given deposition layer thickness would be compared. This would be demonstrated at different temperatures, and the percentage deviation from the theoretical model would be determined.

It will be shown both theoretically and experimentally that there exists a correlation for distinguishing thickness variation as a function of varying group velocities for different frequencies at different temperatures. Feasibility and applicability of TAP-NDE and Gabor Wavelet Transform to thickness examination at elevated temperatures on silicon wafer processing would thus be demonstrated, and the groundwork for a Lamb wave interrogation system for silicon wafer analysis would be established.

CHAPTER II

THEORY

SILICON CRYSTALLOGRAPHY

A fundamental knowledge of crystal orientation in the Silicon wafer is necessary to understand further concepts in developing a theoretical model for analysis. Single crystal silicon is available as wafers of varying diameter, thickness, orientation, dopant, and resistivity. The Miller Indices denote the plane or direction of a periodic arrangement of atoms in a lattice. A cubic lattice would have Miller indices as either [100], [110] or [111]. A form, group or family of faces that bear similar relationships to the crystallographic axes are equivalent, and can be denoted by the same indices.

Crystalline Silicon has a covalently bonded structure, with tetrahedral orientation, making it similar to carbon in the diamond form. The structure is face centered cubic, with two atoms in the unit cell. Silicon wafers for the IC industry are commonly made in the [100] and the [110] orientation, and the [100] orientation would be used for this study. The orientation on a wafer is made evident by an orientation flat, which is a flat segment of the piece. The wafer would normally carry two flats, a primary flat that depicts the orientation, and the secondary flat, that identifies conductivity type. In this study, wafers of [100] orientation with a secondary flat at the [110] orientation would be used (Figure 2-1). Silicon is also chosen as a substrate for wafers because of its intrinsic mechanical stability, and its advantages in terms of machineability, and metallization ease, and implementation of small features on the substrate. Any mechanical sensor application would require the integration of the mechanical, electromechanical and electrical transfer functions.

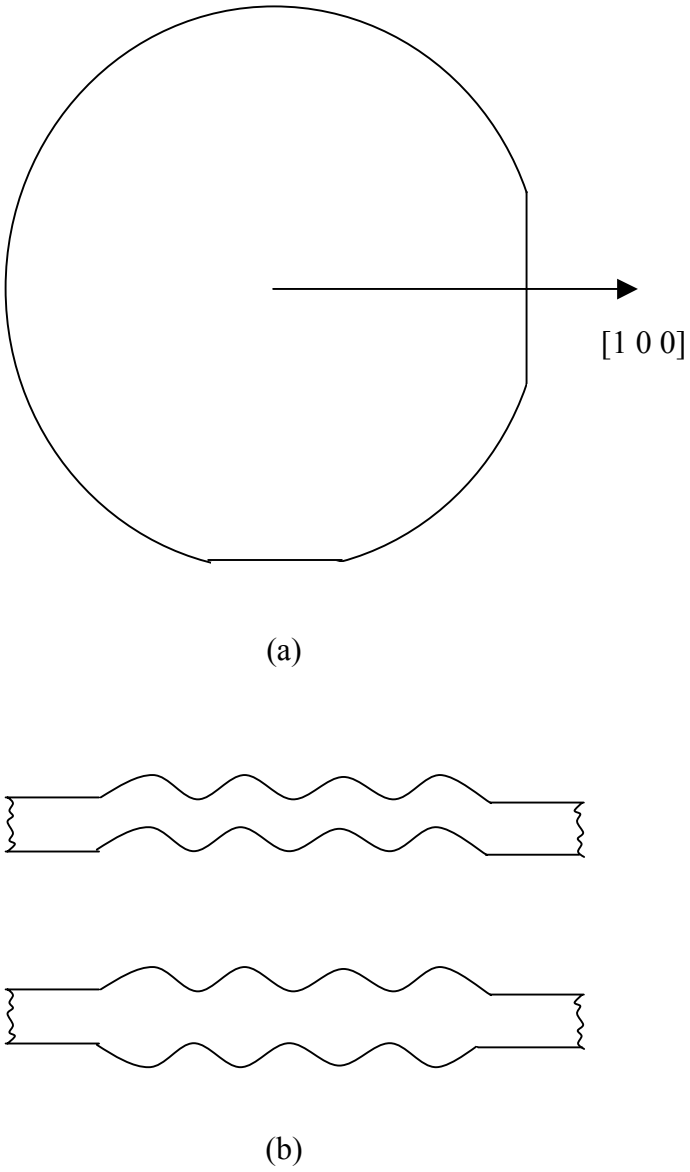

Figure 2-1 (a) Primary and secondary flats on [100] p-type Silicon wafer, and (b) symmetric and anti-symmetric waves on the wafer

These transfer functions are defined and optimized using mechanical models with the independent elastic constants as the input parameters. An isotropic material can be characterized by two independent elastic constants, while an anisotropic material has its independent elastic constants increasing with decreasing symmetry.

Any sensor should have minimal drift in values to avoid recalibrations. In ductile materials, dislocations can readily move about, while in brittle materials like Silicon, which can be made with virtually no defects, dislocations hardly move. Thus, at room temperature Silicon can be deformed only elastically. Single crystal silicon also has a high thermal conductivity, with a low thermal expansion. With increasing temperature, its elastic modulus diminishes. Moreover, Silicon has a high yield strength, which makes it the best-suited structural element for IC applications.

ORTHOTROPIC PLATE WAVE DISPERSION

In the case of elastic perturbations in a plate of finite thickness, displacements occur both in the direction of wave propagation, and perpendicular to the plane of the plate. These two dimensional elastic stress waves are termed as Lamb waves, and are guided by the surface boundary that serves as a waveguide. For a fixed frequency in a plate of thickness 2d, there exist a finite number of symmetric and anti-symmetric modes of propagation, that differ in phase and group velocities and have varying stress and displacement distributions across the cross section. The higher the mode, the higher its cut-off value is in terms of frequency. The lowest modes are shown as A_o and S_o, which represent the anti-symmetric and symmetric modes correspondingly. Lamb waves are highly dispersive in nature as the excitation source is broadband, and carries a number of different frequency components propagating at different velocities. This makes it difficult to measure the phase velocity of the different modes.

An infinite isotropic medium would permit dilatational and distortional waves, both of which are non-dispersive. However, if a dilatational or a distortional wave is reflected from a free boundary, partial mode conversion occurs. This interference of multiple reflections, and subsequent mode conversion eliminates the existence of pure bulk modes. In terms of modeling, Silicon wafers obey an anisotropic elastic description in the corresponding crystal axes orientations. The relation between stresses and strains is more complex, and depends on the spatial orientation with respect to the crystallographic axes. Hooke's law in the most generic form is given as

$$\sigma_{ij} = E_{ijkl}\varepsilon_{kl} \qquad (2-1)$$

The stress and strain tensors from the above equation can be rewritten as

$$\sigma_m = \sum_{n=1}^{6} E_{mn}\varepsilon_n \qquad (2-2)$$

The components of the tensor E_{mn} can be substituted to generate the final stiffness matrix. The elements of this matrix are governed by different factors like crystal and element symmetry. For

$$\begin{bmatrix} \sigma_{11} \\ \sigma_{22} \\ \sigma_{33} \\ \sigma_{23} \\ \sigma_{13} \\ \sigma_{12} \end{bmatrix} = \begin{bmatrix} C_{11} & C_{12} & C_{12} & 0 & 0 & 0 \\ C_{12} & C_{11} & C_{12} & 0 & 0 & 0 \\ C_{12} & C_{12} & C_{11} & 0 & 0 & 0 \\ 0 & 0 & 0 & 2C_{44} & 0 & 0 \\ 0 & 0 & 0 & 0 & 2C_{44} & 0 \\ 0 & 0 & 0 & 0 & 0 & 2C_{44} \end{bmatrix} \begin{bmatrix} \varepsilon_{11} \\ \varepsilon_{22} \\ \varepsilon_{33} \\ \varepsilon_{23} \\ \varepsilon_{13} \\ \varepsilon_{12} \end{bmatrix} \qquad (2-2)$$

an isotropic medium, these independent constants number only two, while for an anisotropic orthotropic medium such as the wafer substrate under consideration, the stiffness coefficient matrix would have three independent elastic constants, C_{11}, C_{12}, and C_{44}, which gives the Hooke's law as Equation $(2-3)$.

The objective is to study the behavior of elastic waves on silicon wafers with deposition layers on it, and at different temperatures. In this study, wafers with aluminum and copper deposition layers, with a relatively small layer of titanium as the barrier material has been used. In developing an analytical model, the lattices of the deposition layers have to be studied along with the substrate.

Aluminum and copper exhibit the same cubic lattice structure as silicon, while titanium is known to exhibit a hexagonal crystal lattice structure. The stiffness matrix for a hexagonal lattice would have five independent elastic constants, and Hooke's Law can be expressed as

$$Stiffness = \begin{bmatrix} C_{11} & C_{11}-2C_{66} & C_{13} & 0 & 0 & 0 \\ C_{12}-2C_{66} & C_{11} & C_{13} & 0 & 0 & 0 \\ C_{13} & C_{13} & C_{33} & 0 & 0 & 0 \\ 0 & 0 & 0 & C_{44} & 0 & 0 \\ 0 & 0 & 0 & 0 & C_{55} & 0 \\ 0 & 0 & 0 & 0 & 0 & C_{66} \end{bmatrix} \qquad (2-4)$$

The values of each of these independent elastic constants have been predetermined, and will be used for developing the model. Habeger et. all [8] formulated the dispersion equation for an orthotropic plate in a general form using the elastic constants as shown above. The formulation is for a fixed plane of symmetry, and its extension to the current work can be understood as follows for a stand-alone substrate, and for a wafer with deposition layers on it.

STRAIN - DISPLACEMENT RELATION

On considering a cube subjected to an elastic deformation, the strain tensor relating to the cube element can be derived in terms of the corresponding normal and shear strain components. The strain tensor is given by

$$\begin{bmatrix} \varepsilon_{xx} & \gamma_{xy} & \gamma_{xz} \\ \gamma_{yx} & \varepsilon_{yy} & \gamma_{yz} \\ \gamma_{zx} & \gamma_{zy} & \varepsilon_{zz} \end{bmatrix} \tag{2-5}$$

Strain is defined in terms of displacement, and hence each term of the strain tensor can be rephrased as related to displacement. For infinitesimally small displacements, it can be seen that the final displacement vector U_f is related to the initial displacement vector U_i by the small stretch of the element ($\partial U/\partial x$) in that axial direction, as

$$U_f = \frac{\partial U}{\partial x} U_i + U_i \tag{2-6}$$

Since strain is defined as the ratio of change in displacement to the original displacement vector, it can be rewritten in the following form after substituting the above relation

$$\varepsilon = \frac{U_f - U_i}{U_i} = \frac{\partial U}{\partial x} \tag{2-7}$$

Normal strain in each of the axial directions can thus be written in terms of displacement. The shear strain components of the tensor are slightly more complicated, as it accounts for the angular rotations of the corresponding control elements. Shear strain is related to rotation as

$$\gamma = \frac{1}{2}(\theta_1 + \theta_2) \tag{2-8}$$

Where θ_1 and θ_2 are the angles by which each side of the control element is deformed towards the related diagonal. For infinitesimally small angular deformations, the sinusoidal components can be replaced by the angles, and thus, the shear strain component can be stated as

$$\gamma_{xy} = \frac{1}{2}\left(\frac{\partial U}{\partial y} + \frac{\partial V}{\partial x}\right) \tag{2-9}$$

The final strain tensor matrix thus becomes

$$\begin{bmatrix} \dfrac{\partial U}{\partial x} & \dfrac{1}{2}\left(\dfrac{\partial U}{\partial y}+\dfrac{\partial V}{\partial x}\right) & \dfrac{1}{2}\left(\dfrac{\partial U}{\partial z}+\dfrac{\partial W}{\partial x}\right) \\ \dfrac{1}{2}\left(\dfrac{\partial V}{\partial x}+\dfrac{\partial U}{\partial y}\right) & \dfrac{\partial V}{\partial y} & \dfrac{1}{2}\left(\dfrac{\partial V}{\partial z}+\dfrac{\partial W}{\partial y}\right) \\ \dfrac{1}{2}\left(\dfrac{\partial W}{\partial x}+\dfrac{\partial U}{\partial z}\right) & \dfrac{1}{2}\left(\dfrac{\partial W}{\partial y}+\dfrac{\partial V}{\partial z}\right) & \dfrac{\partial W}{\partial z} \end{bmatrix} \qquad (2-10)$$

In indicial notation, the matrix representation of strain in terms of displacements is stated as

$$\varepsilon_{ij} = \frac{1}{2}\left(\frac{\partial U_i}{\partial x_j}+\frac{\partial U_j}{\partial x_i}\right) = \frac{1}{2}\left(U_{i,j}+U_{j,i}\right) \text{ for i = 1,2,3} \qquad (2-11)$$

STRESS - DISPLACEMENT RELATION

The stress tensor is given by

$$\begin{bmatrix} \sigma_{xx} & \tau_{xy} & \tau_{xz} \\ \tau_{yy} & \sigma_{yy} & \tau_{yx} \\ \tau_{zx} & \tau_{zy} & \sigma_{zz} \end{bmatrix} \qquad (2-12)$$

If t_i is the traction component, it is related to the stress tensor by

$$t_i = \sigma_{ij} n_j \qquad (2-13)$$

Conservation of momentum states that the rate of change of momentum is equal to the total force acting on the body, and hence can be written as

$$\frac{D}{Dt}\int_{\mathrm{V}} \mathrm{V_i}\,\rho dV = \int_S t_i dS + \int_V f_i \rho dV \qquad (2-14)$$

Where v_i is the velocity of every point associated with the medium, ρ is the mass density per unit volume of the medium, and f_i is the body force associated with the medium.

Green-Gauss theorem is expressed in Cartesian form as

$$\int_V U_{j,j}\,dV = \int_S U_j n_j\,dS \qquad (2-15)$$

Thus the surface integral of Equation $(2-14)$ can be rewritten in terms of volume integral, to give

$$\int_V (\rho \overset{\circ\circ}{U}_i - \sigma_{ji,j} - \rho f_i)\,dV = 0 \qquad (2-16)$$

Since V is arbitrary and neglecting body forces, the above equation can be rearranged to relate the stress tensor to the displacement as

$$\sum_{j=1}^{3} \sigma_{ij,j} = \rho \overset{\circ\circ}{U}_i \qquad \text{for i = 1,2,3} \qquad (2-17)$$

This gives the equation of motion for a mechanical disturbance in an elastic medium.

PLATE WAVE SOLUTION

Bulk waves propagating in the x-z plane are to be studied. Hence the displacement in the y-direction, and all its derivatives pertinent to the y-direction should be zero. For the x-direction, the *i* value is 1 in Equation $(2-17)$, and thus,

$$\rho \overset{\circ\circ}{U}_i = \sum_{j=1}^{3} \sigma_{ij,j} = \sigma_{11,1} + \sigma_{13,3} \qquad (2-18)$$

From Hooke's law, the expression for σ_{11} and σ_{13} is found to be

$$\sigma_{11} = C_{11}\varepsilon_{11} + C_{13}\varepsilon_{33} \qquad (2-19)$$

$$\sigma_{13} = 2C_{55}\varepsilon_{13} \qquad (2-20)$$

Using the relation between strain and displacement from Equation $(2-11)$, the above relations can be rewritten as

$$\sigma_{11} = C_{11}U_{1,1} + C_{13}U_{3,3} \qquad (2-21)$$

$$\sigma_{13} = C_{55}(U_{1,3} + U_{3,1}) \qquad (2-22)$$

Equation $(2-18)$ becomes

$$\rho \overset{\circ\circ}{U}_i = C_{11}U_{1,11} + C_{13}U_{3,31} + C_{55}(U_{1,33} + U_{3,13}) \qquad (2-23)$$

Similarly the expression for the z-direction is found to be

$$\rho \overset{\circ\circ}{U}_i = C_{33}U_{3,33} + C_{13}U_{1,13} + C_{55}(U_{1,13} + U_{3,11}) \qquad (2-24)$$

For the solutions to represent the plane waves,

$$U_1 = U_{10} \exp\left[i\left(k_x x + k_z z - \omega t\right)\right] \qquad (2-25)$$

$$U_3 = U_{30} \exp\left[i\left(k_x x + k_z z - \omega t\right)\right] \qquad (2-26)$$

where U_{10} and U_{30} are the amplitude of oscillations. By simplifying the expressions obtained by substituting the above solutions in Equation $(2-21)$ and Equation $(2-22)$, it is possible to determine the different values of k_z and the corresponding U_{30} / U_{10} values. This is determined by first determining the values of k_z that satisfy the following quadratic equation

$$\begin{aligned}\left(C_{55} + C_{13}\right)^2 k_x{}^2 k_z{}^2 = &\left(\rho\omega^2 - C_{11}k_x{}^2 - C_{55}k_z{}^2\right) \\ &\times \left(\rho\omega^2 - C_{55}k_x{}^2 - C_{33}k_z{}^2\right)\end{aligned} \qquad (2-27)$$

The k_z values thus determined are substituted to obtain the value of U_{30} / U_{10} as

$$\frac{U_{30}}{U_{10}} = \frac{\left(\rho\omega^2 - C_{11}k_x{}^2 - C_{55}k_z{}^2\right)}{\left(C_{55} + C_{13}\right)k_x k_z} \qquad (2-28)$$

Different values of k_z that are solutions to the quadratic equation can be used to demonstrate that orthotropic bulk waves propagate similar to isotropic bulk waves, by showing that the two plate solutions possess disturbances that are either normal or parallel to the direction of wave propagation.

Waves that propagate at an angle to either the x or z-axis have disturbances neither normal nor parallel to the travel direction. This more generalized case gives a coupled equation in terms of k_x^2 and k_z^2 as

$$k_z{}^2 \pm = \frac{k_x{}^2}{2}\left[-B \pm \sqrt{B^2 \pm 4D}\right] \tag{2-29}$$

where

$$B = \frac{\rho}{C_{33}C_{55}}\left[C_{33}\left(\frac{C_{11}}{\rho} - \frac{\omega^2}{k_x{}^2}\right) - C_{13}\left(\frac{2C_{55}+C_{13}}{\rho}\right) - C_{55}\frac{\omega^2}{k_x{}^2}\right] \tag{2-30}$$

$$D = \frac{\rho^2}{C_{33}C_{55}}\left(\frac{\omega^2}{k_x{}^2} - \frac{C_{55}}{\rho}\right)\left(\frac{\omega^2}{k_x{}^2} - \frac{C_{11}}{\rho}\right) \tag{2-31}$$

There exist two solutions for k_z^2 from the above equation for a given value of frequency and k_x, which in turn yields four possible solutions to k_z. This gives the possible bulk waves that propagate through an orthotropic medium. For the solid elastic plate, any combination of these four waves can be a wave in the x direction. Thus, different combinations can be evaluated that satisfy the free boundary conditions of the plate. A solution for the propagating wave can exist only for specific combinations of frequency and wave number k_x. Thus, the plate wave solutions can be expressed as

$$U_1 = \exp\left[i\left(k_x x - \omega t\right)\right]\begin{bmatrix} M\exp\left(ik_{z+}z\right) + N\exp\left(-ik_{z+}z\right) \\ + P\exp\left(-ik_{z-}z\right) + Q\exp\left(-ik_{z-}z\right)\end{bmatrix} \tag{2-32}$$

$$U_3 = \exp\left[i\left(k_x x - \omega t\right)\right]\begin{bmatrix} \tan\phi + M\exp\left(ik_{z+}z\right) - N\exp\left(-ik_{z+}z\right) \\ + \tan\phi - P\exp\left(-ik_{z-}z\right) - Q\exp\left(-ik_{z-}z\right)\end{bmatrix} \tag{2-33}$$

There exist zero stress conditions at the free boundary z = ±b, which implies that

$$\tau_{33} = C_{33}U_{3,3} + C_{13}U_{1,1} = 0 \tag{2-34}$$

$$\tau_{31} = C_{55}U_{1,3} + C_{55}U_{3,1} = 0 \qquad (2-35)$$

By substituting the plate wave solutions into the boundary conditions, and simplifying, we get

$$\begin{bmatrix} G_+\exp(ik_{z+}b) & G_+\exp(-ik_{z+}b) & G_-\exp(ik_{z-}b) & G_-\exp(-ik_{z-}b) \\ G_+\exp(-ik_{z+}b) & G_+\exp(ik_{z+}b) & G_-\exp(-ik_{z-}b) & G_-\exp(ik_{z-}b) \\ H_+\exp(ik_{z+}b) & -H_+\exp(-ik_{z+}b) & H_-\exp(ik_{z-}b) & -H_-\exp(-ik_{z-}b) \\ H_+\exp(-ik_{z+}b) & -H_+\exp(ik_{z+}b) & H_-\exp(-ik_{z-}b) & H_-\exp(ik_{z-}b) \end{bmatrix} \begin{bmatrix} M \\ N \\ P \\ Q \end{bmatrix} = 0 \qquad (2-36)$$

where

$$G_\pm = C_{33}k_{z\pm}\tan\Phi_\pm + C_{13}k_x \qquad (2-37)$$

$$H_\pm = k_{z\pm} + k_x\tan\Phi_\pm \qquad (2-38)$$

The above equation can generate solutions to the wave only if the determinant of the above matrix is zero. Thus, the solution to the dispersion equation for an orthotropic plate wave is given by

$$\frac{\tan(k_{z+}b)}{\tan(k_{z-}b)} = \left[\frac{H_-G_+}{H_+G_-}\right]^{\pm 1} \qquad (2-39)$$

The symmetric modes correspond to the +1 exponent in the above expression, while the anti-symmetric modes are given by solving the above equation with the -1 exponent.

GRAPHICAL SIMULATION

The location of the proper wave number region where a mode's particular frequency component exists can be determined by using graphical simulation of the above theoretical formulation. The different modes of wave propagation are functions of frequency and wave number k_x. To obtain the symmetric and anti-symmetric modes, the determinant of the matrix from Equation

$(2-36)$ should become zero. Depending upon the plus or minus signs indicated for the symmetric or anti-symmetric modes, the corresponding modes could be generated.

A FORTRAN code was used to generate the plots [Appendix B]. The input parameters were the elastic constants, the density and thickness of the substrate wafer, the frequency and wave number range, and the operating temperature of the system. The resulting symmetric and anti-symmetric modes for a substrate wafer of 525 microns thickness are shown in Figure 2-2(a) and Figure 2-2(b) respectively.

The group velocity, given by $\Delta\omega/\Delta k$, is equal to the phase velocity ($c=\omega/k$) for the Rayleigh mode that is seen as a straight line. For different modes, the group and phase velocity can be seen to change for different frequencies, as observed from the varying slope of the curves. The higher modes in each case can also be observed. The dependence of temperature to the S_o and A_o modes in silicon wafer processing has been demonstrated by Rabroker [13] in a detailed study of laser induced stress wave thermometry. All the modes were shown to shift downward with an increase in temperature, as shown in Figure 2-3. With a further increase in temperature, the modes will be observed to shift further downward, following the same trend as seen in Figure 2-3. It is also to be noted that there is a small gap in one of the higher modes because of the coarse resolution in terms of wave number that was used in the code, which was insufficient to yield a suitable solution to remove the disjoint seen in the figure.

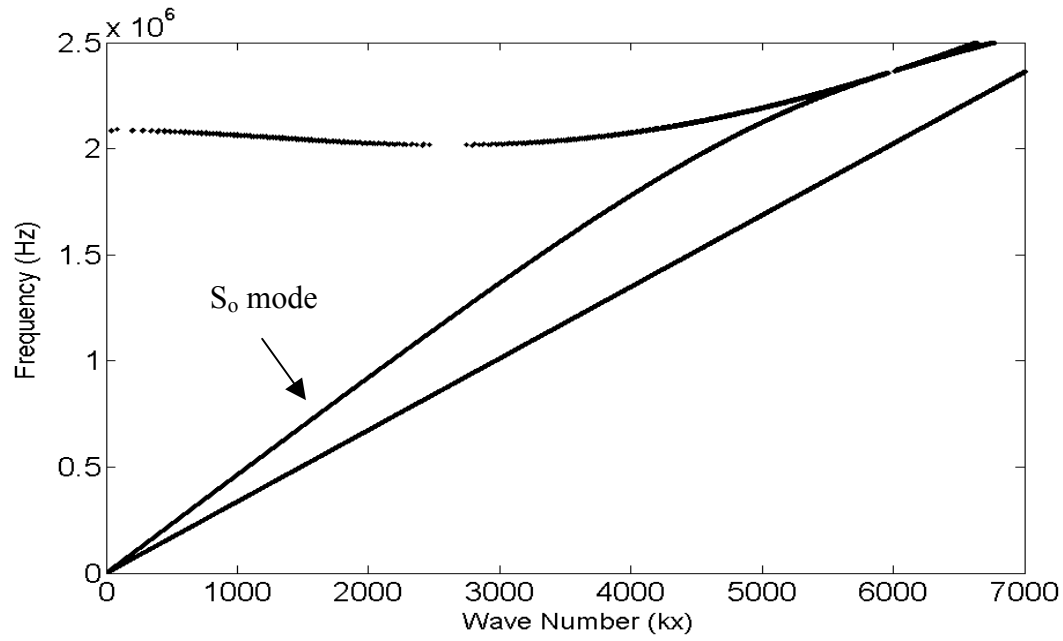

(a)

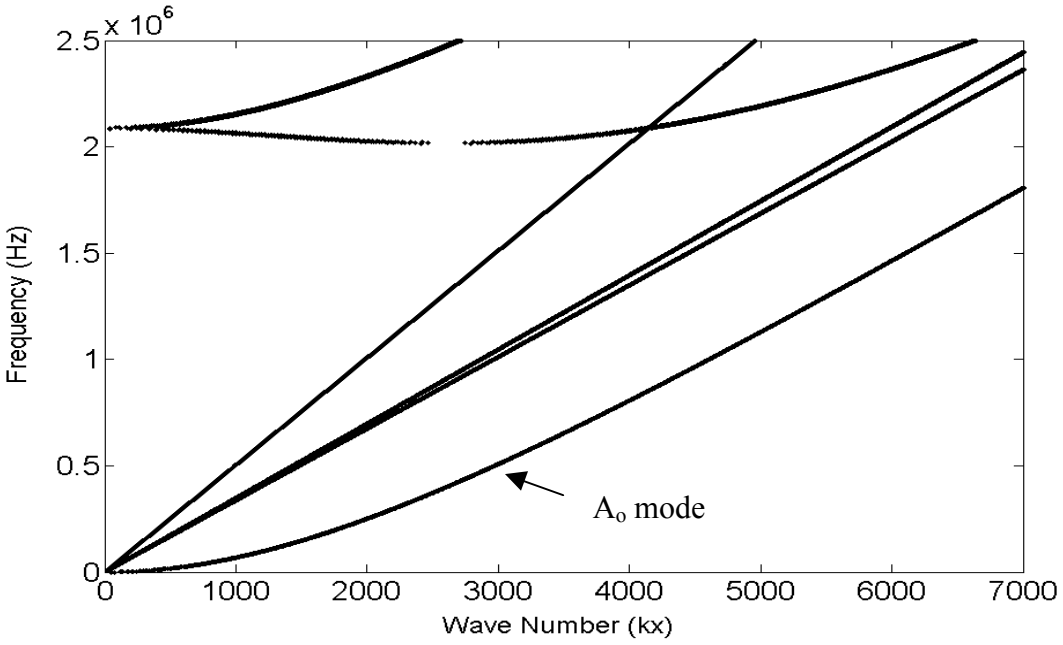

(b)

Figure 2-2 (a) Symmetric modes on [1 0 0] orientation, and (b) anti-symmetric modes on [1 0 0] orientation

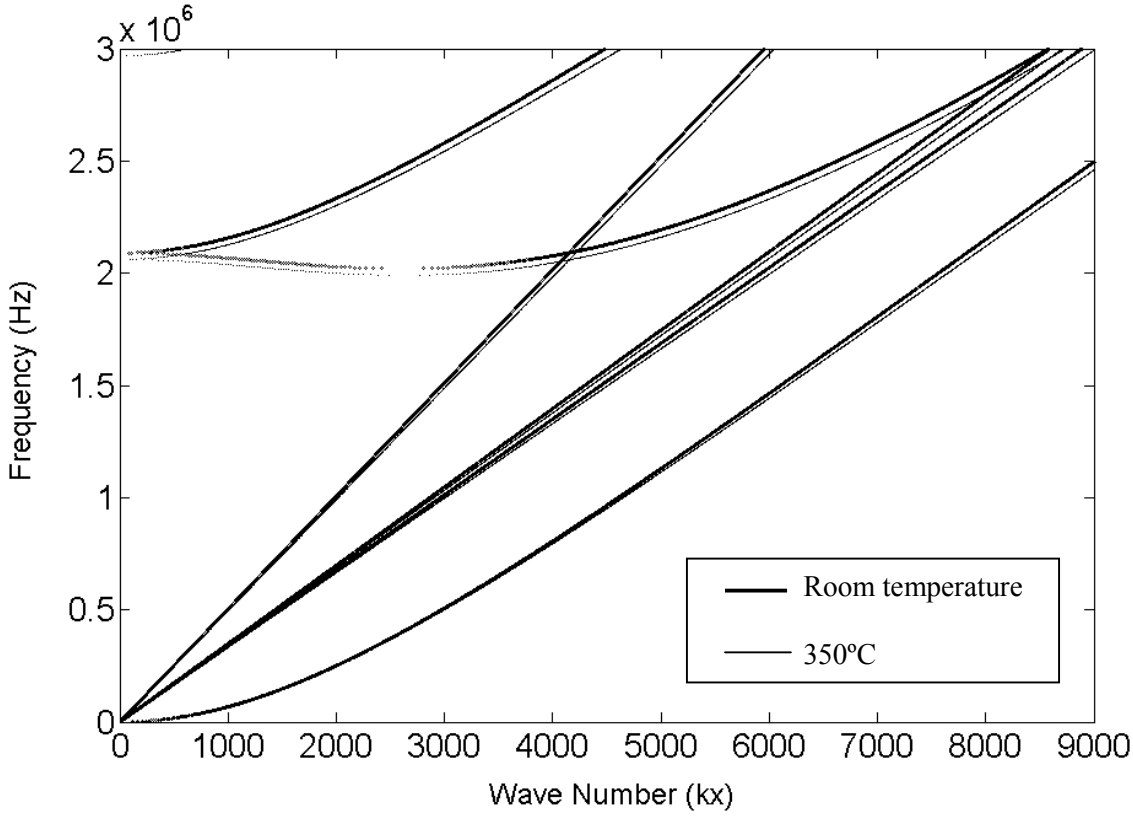

Figure 2-3 Anti-symmetric modes for room temperature (25ºC) and 350ºC

DEPOSITION LAYER EFFECTS

It can be clearly seen that the elastic constants play a major role in the determination of the phase and group velocity of a propagating wave. Any changes to the elastic constants will yield a different set of frequency-wave number solutions to the dispersion equation. This forms the basis for analysis of the effects of deposition layer thickness on the dispersion curves, and the corresponding group velocities.

Grimsditch [10] derived a generalized form for determination of the effective elastic constants for a system with multiple layers, each exhibiting an orthorhombic symmetry about its principal axes along the super lattice axis. The formulation used here for deposition layer thickness modeling has been adopted from the derivation of the effective elastic constants by Grimsditch [10].

In general, for a super lattice with its axis along the z-direction, the diagonal and off-diagonal components of σ and μ do not couple with each other. If the top layer thickness is d_1, and the second layer thickness is d_2, then the fraction of each layer is given by

$$f_i = \frac{d_1}{d_1 + d_2} \tag{2-40}$$

where f_i is the fractional thickness of each layer. From the symmetry, the following relations for stress and strain hold good

$$\left.\begin{aligned} \sigma_{zz} &= \sigma_{zz}^1 = \sigma_{zz}^2 \\ \sigma_{xx} &= f_1\sigma_{xx}^1 + f_2\sigma_{xx}^2 \\ \sigma_{yy} &= f_1\sigma_{yy}^1 + f_2\sigma_{yy}^2 \\ \mu_{zz} &= f_1\mu_{zz}^1 + f_2\mu_{zz}^2 \\ \mu_{xx} &= \mu_{xx}^1 = \mu_{xx}^2 \\ \mu_{yy} &= \mu_{yy}^1 = \mu_{yy}^2 \end{aligned}\right\} \tag{2-41}$$

Considering the relations for effective elastic constants from Hooke's law

$$\sigma_{zz} = C_{33}\mu_{zz} + C_{13}\mu_{xx} + C_{23}\mu_{yy} \qquad (2-42)$$

Evaluating partial fractions for the corresponding layer, it is possible to compare the coefficients of the strain components to give

$$C_{33} = \left[\frac{f_1}{C_{33}^1} + \frac{f_2}{C_{33}^2}\right]^{-1} \qquad (2-43)$$

$$C_{13} = \frac{f_1 C_{13}^1 C_{33}^2 + f_2 C_{13}^2 C_{33}^1}{f_1 C_{33}^2 + f_2 C_{33}^1} \qquad (2-44)$$

$$C_{23} = \frac{f_1 C_{23}^1 C_{33}^2 + f_2 C_{23}^2 C_{33}^1}{f_1 C_{33}^2 + f_2 C_{33}^1} \qquad (2-45)$$

$$C_{11} = f_1 C_{11}^1 + f_2 C_{11}^2 + f_1 \frac{C_{13}^1}{C_{33}^1}(C_{13} - C_{13}^1) + f_2 \frac{C_{23}^1}{C_{33}^2}(C_{13} - C_{13}^2) \qquad (2-46)$$

$$C_{12} = f_1 C_{12}^1 + f_2 C_{12}^2 + f_1 \frac{C_{13}^1}{C_{33}^1}(C_{13} - C_{13}^1) + f_2 \frac{C_{23}^1}{C_{33}^2}(C_{13} - C_{13}^2) \qquad (2-47)$$

Evaluating by elimination, and simplifying, the above relations give

$$C_{22} = f_1 C_{22}^1 + f_2 C_{22}^2 + f_1 \frac{C_{23}^1}{C_{33}^1}(C_{23} - C_{23}^1) + f_2 \frac{C_{23}^1}{C_{33}^2}(C_{23} - C_{23}^2) \qquad (2-48)$$

The shear components can be evaluated in a similar fashion to give

$$C_{44} = \left[\frac{f_1}{C_{44}^1} + \frac{f_2}{C_{44}^2}\right]^{-1} \qquad (2-49)$$

$$C_{55} = \left[\frac{f_1}{C_{55}^1} + \frac{f_2}{C_{55}^2}\right]^{-1} \qquad (2-50)$$

$$C_{66} = \left[\frac{f_1}{C_{66}^1} + \frac{f_2}{C_{66}^2}\right]^{-1} \qquad (2-51)$$

The above equations list the nine independent effective elastic constants for a super lattice with orthorhombic symmetry. Using the effective elastic constants for the required combinations of deposition layers and the substrate on the orthotropic plate wave dispersion equation, it is possible to determine the k_x values for different frequency values. This would yield the corresponding dispersion curves that depict the symmetric and anti-symmetric modes for each case.

NUMERICAL SIMULATION

As established earlier, the effective elastic moduli can be determined for each type of wafer that forms a part of the sample. Based on the formulation for the dispersion equation, the corresponding symmetric and anti-symmetric modes for each case can be obtained by plotting frequency as a function of wave number by using the dispersion code [Appendix - B]. The elastic constants for each constituent metal and silicon for varying temperatures are obtained from a handbook for elastic constants of single crystals [14].

The assignment of elastic constants based upon the crystal lattice of each element in the considered samples is shown in Table. 2-1. Except for the case of silicon, the elastic constants at elevated temperatures for all the other elements are obtained from the handbook [14]. The elastic constants of silicon are found to follow a fairly linear decrease with temperature.

The calculated effective elastic constants for each case are shown in Table. 2-2, where the calculations are based on the previous section. Density for each of the combined systems is calculated as a weighted average of the component densities.

Table 2-1 Elements properties at 25ºC and 350ºC

Element	**Lattice**	**Temperature**	**Density**	**C_{11}**	**C_{13}**	**C_{33}**	**C_{55}**
Silicon	FCC	25ºC	2.331	1.6578	0.6394	1.6578	0.7962
		350ºC	2.331	1.6062	0.61858	1.6062	7.7439
Titanium	HC	25ºC	4.5063	1.624	0.69	1.8070	0.467
		350ºC	4.4700	1.442	0.691	1.678	0.403
Aluminum	FCC	25ºC	2.699	1.0567	0.5897	1.0567	0.2854
		350ºC	2.629	0.9348	0.5724	0.9348	0.2332

Table 2-2 Effective elastic constants for wafer configurations at 25ºC and 350ºC

Wafer Type	**Thickness**	**C_{11} effective**	**C_{13} effective**	**C_{33} effective**	**C_{55} effective**
Silicon Substrate 25ºC	525	1.6578	0.6394	1.6578	0.7962
Silicon Substrate 4000Å Aluminum 250Å Titanium 25ºC	525.425	1.6573	0.63934	1.6571	0.79509
Silicon Substrate 8000Å Aluminum 250Å Titanium 25ºC	525.825	1.6569	0.63928	1.6564	0.79401
Silicon Substrate 350ºC	525	1.6062	0.61858	1.6062	0.77439
Silicon Substrate 4000Å Aluminum 250Å Titanium 350ºC	525.425	1.6057	0.61852	1.6053	0.77299
Silicon Substrate 8000Å Aluminum 250Å Titanium 350ºC	525.825	1.6052	0.61846	1.6045	0.77163

DISPERSION PLOTS FOR ALUMINUM

The numerical simulation as shown in the previous section is used to generate the different modes for the sample configurations of wafers. Figure 2-4 shows the A_o mode from 0 KHz to 80 KHz, which is the zone chosen to demonstrate the change in dispersion with thickness for varying temperature zones. From the plots, it was seen that the thickness resolution is not significant above a frequency range of 80 KHz. The minute changes in thickness, and the total wafer thickness govern the ability to obtain distinct dispersion curves.

Figure 2-5 shows the A_o mode as seen at room temperature and at 350ºC. The effect of deposition layer(s) on the wafer is insignificant as the frequency increases. However, the dispersion curves of the A_o mode diverge with increasing frequency as the temperature increases. The A_o mode is seen to shift to the right with increasing thickness when the frequency range is further shortened. The effects of deposition layers can be clearly observed, where the plain shapes in the figure represent the room temperature A_o mode, while the shaded shapes represent the same mode at a temperature of 350ºC.

The right shift in the A_o mode with increasing thickness of the deposition layer is a reflection of a decrease in the wavelength of the corresponding frequency component. This is seen to happen almost continually all along the 0 KHz to 80 KHz frequency range, though the exhibited pattern is non-linear. Examination of the 20 KHz to 30 KHz regions reveals a zone of compromise between thickness and temperature, where the changes in group velocity would be studied in the next section.

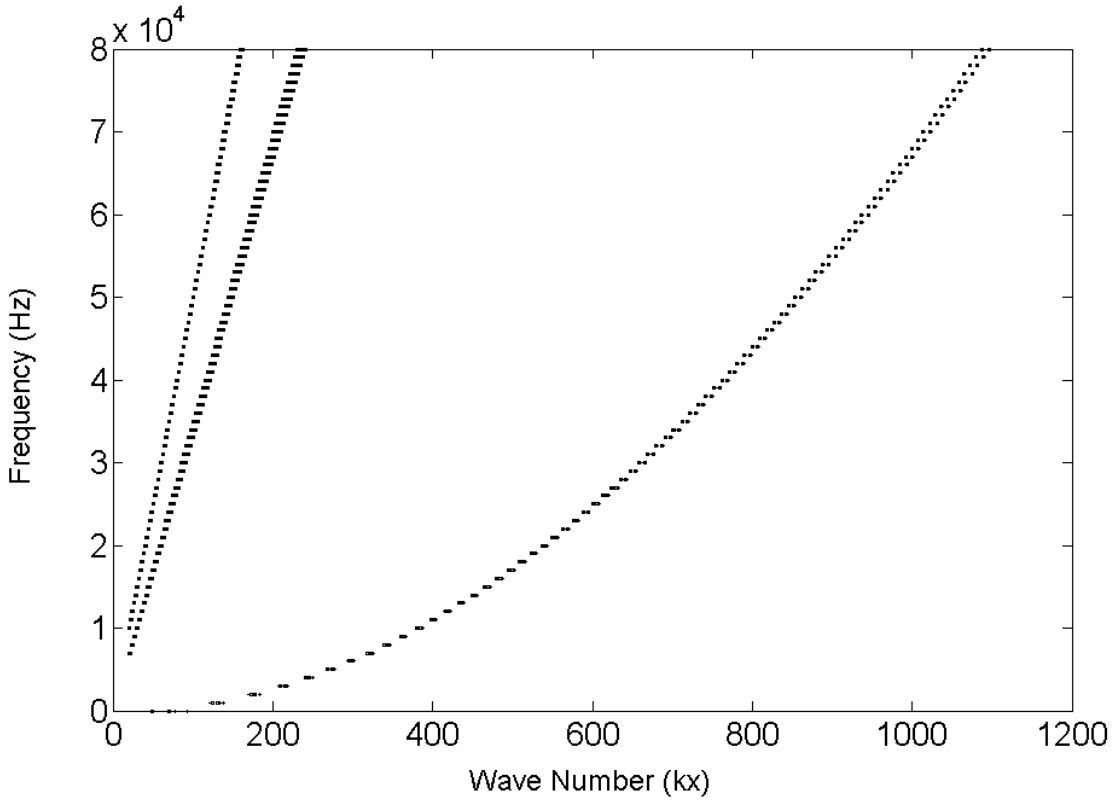

Figure 2-4 Theoretical anti-symmetric modes at room temperature (25ºC) and 350ºC for the 0 - 80 KHz components

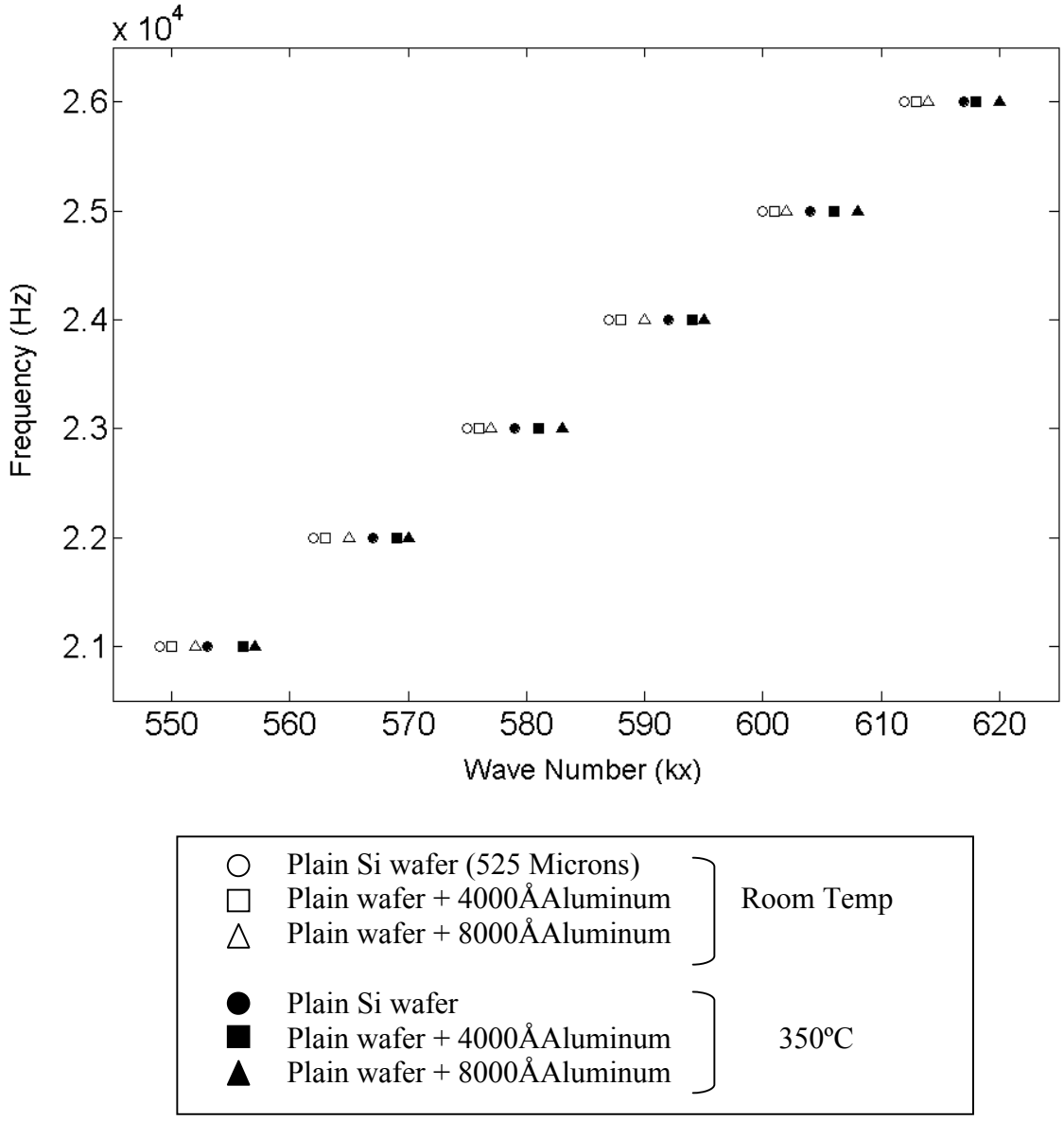

Figure 2-5 Theoretical anti-symmetric modes at room temperature (25ºC) and 350ºC for the 21 - 26 KHz components - detailed illustration

GROUP VELOCITY MODEL

The dispersion observed in the A_o mode is to be converted into a form that is comparable with experimental evaluation of the wafer. Group velocity is one such parameter that can be easily mapped in both the theoretical and experimental domains, and defines the material characteristics distinctly in terms of temperature and frequency changes. Group velocity is also influenced by thickness changes, and will hence be used to evaluate the error levels in values between theoretical and experimental results.

Group velocity determination is done using the FORTRAN code [Appendix C]. The governing parameters are once again seen to be the effective elastic constants, and the frequency at which the group velocity calculations are desired. The wave number band where the frequency is seen is obtained from the dispersion model. The change in the group velocity is seen as a function of increasing temperature, for a fixed value of frequency and thickness. In this thesis, the group velocity model has been developed up to a temperature range of 600ºC, as the material property data, in terms of elastic constants, and density, are available only till that range.

Figure 2-6 shows the group velocity plot for each frequency value from 10 KHz to 60 KHz for a temperature range up to 600ºC. At each frequency level, the group velocities as observed in each of the three kinds of wafers is shown as distinct curves. It can also be seen that as temperature increases, the group velocity plot of the three wafers for any one particular frequency belt diverges. The slopes of the lines are also seen to be negative, suggesting a drop in the group velocity as temperature increases.

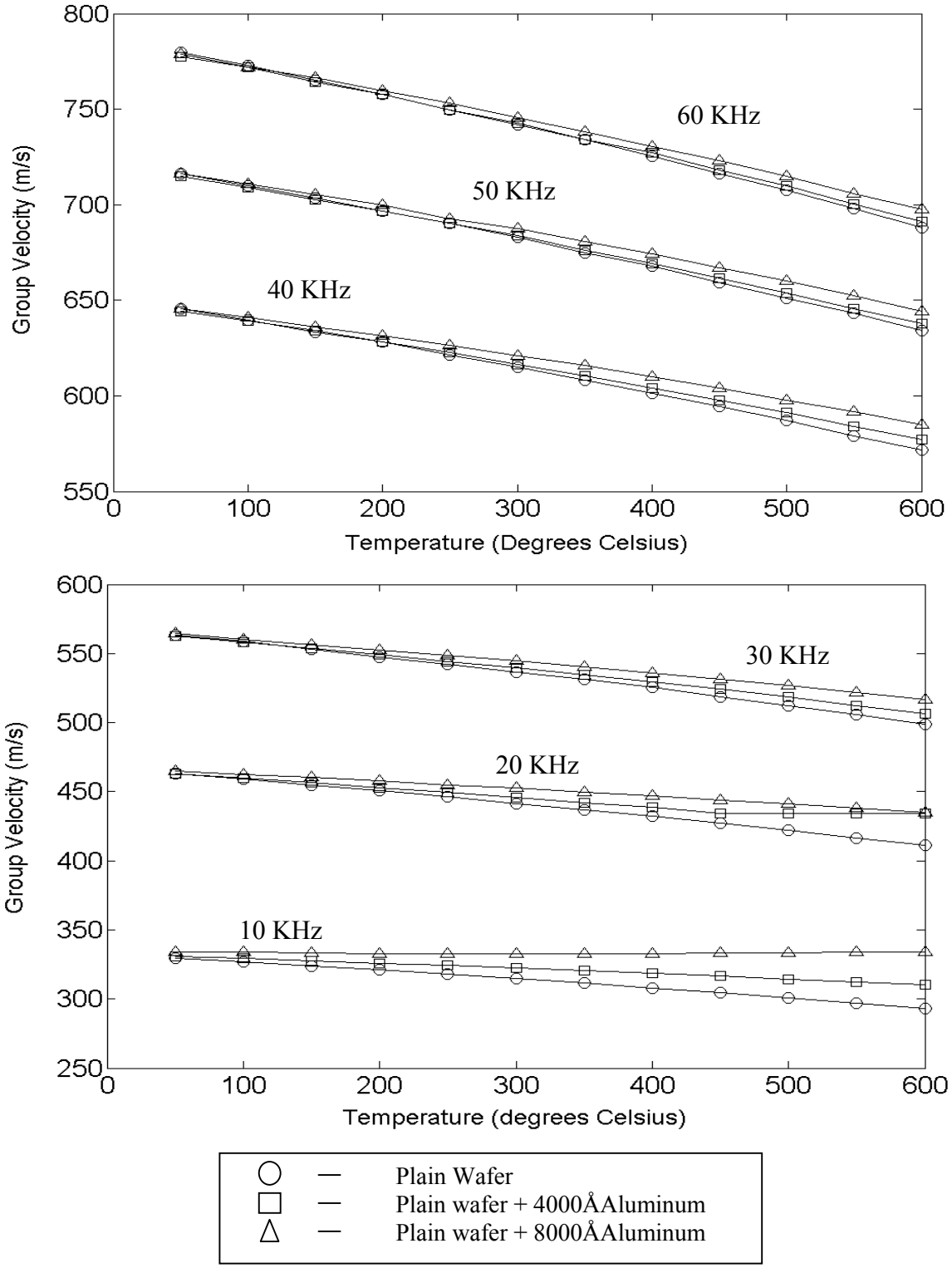

Figure 2-6 Group velocity plots for 10 KHz - 60 KHz frequencies from room temperature to 600ºC for the three different types of wafers

SIMULTANEOUS TEMPERATURE AND THICKNESS CHARACTERIZATION

As seen above, it is possible to identify the change in group velocity for different frequency bands, so as to demonstrate a change in thickness, and also a change in temperature. In other words, a wafer with a specific thickness will demonstrate a particular group velocity distribution for different temperatures, and that this distribution has an increasing slope with increasing frequency. Similarly, for a particular temperature as seen in Figure 2-6, different thickness wafers demonstrate different group velocities of the propagating wave. It is to be noted here, that the resolution of thickness differentiation is higher at lower frequencies.

It is desired in the industry, to simultaneously examine temperature and thickness. Since both thickness and temperature are coupled parameters that simultaneously influence group velocity, it becomes necessary to examine two frequency bands for each wave pulse, one to achieve temperature resolution, and the other, to obtain thickness differentiation. Identification of the right frequency band for each of the above two cases can be achieved by examining the dispersion models for the pattern with which temperature and thickness get affected.

Upon examination of the dispersion model at different frequency ranges, it was found that the A_o mode displays an increasingly diverging characteristic for temperature. In other words, with increasing frequency, temperature resolution becomes easier to achieve. This is shown in Figure 2-7(a). The figure shows how the A_o mode diverges in terms of temperature distribution, with increasing frequency. The bands shown refer to room temperature, and 350ºC. As seen at lower frequencies (20 KHz - 40 KHz), the two bands are not clearly distinguishable. However, with increasing frequencies (60 KHz and above), there exist two clear bands, which diverge with increasing frequency. It can thus be concluded that in order to map temperature accurately, a frequency of around 70 KHz to 80 KHz could be selected for analysis.

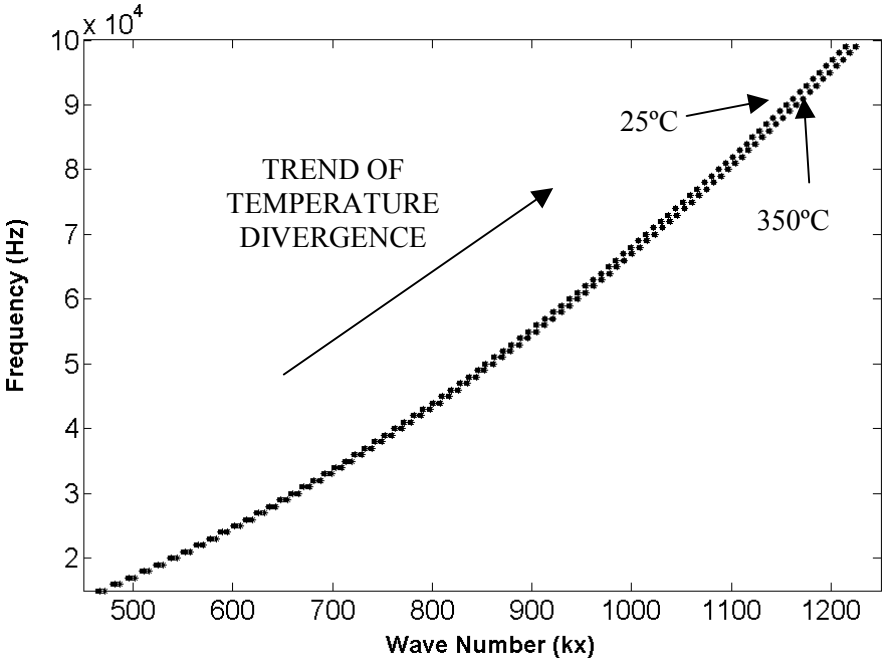

(a)

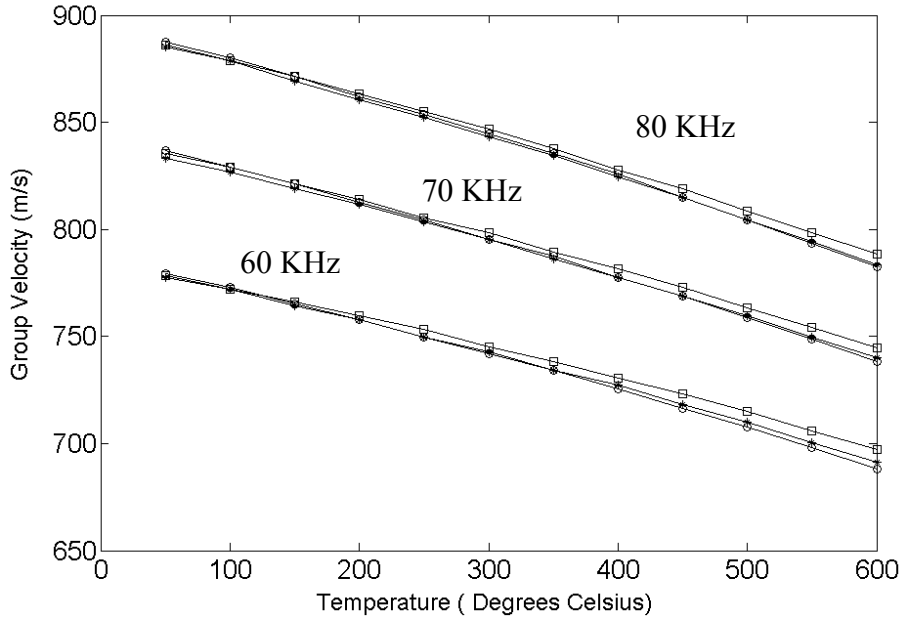

(b)

Figure 2-7 (a) Dispersion model showing divergence of temperature bands with increasing frequency, and (b) comparison of three higher frequency bands showing increasing slopes at higher frequencies (NOTE: legend for different thickness as shown in Figure 2-6)

The group velocity model for the 60 KHz to 80 KHz band is shown in Figure 2-7(b). As seen in the figure, the slope of the group velocity distribution increases with increasing frequency. In turn, it indicates that the change in group velocity for a unit rise in temperature is higher for higher frequencies. Thus, distinguishing between consecutive unit changes in temperature becomes easier at higher frequencies. Generation of higher frequency ranges would prove to ease the possibility of temperature resolution, but is limited by the wavelength of generation.

On a similar basis, the ability to differentiate thickness is examined using the dispersion model first. On doing so, it is seen as shown in Figure 2-8(a) that the lower frequencies show a more pronounced effect of thickness differentiation than higher frequencies. The effect is lesser in terms of resolution in the figure, because of the minute variation in thickness, and also the rather non-linear distribution of the pattern with changing frequencies. However, it was observed that at a low frequency of about 15 KHz to 25 KHz, the distribution of thickness patterns could be mapped into a corresponding identifiable distribution in terms of group velocity.

As seen in the group velocity model in Figure 2-8(b), it is possible to achieve a good resolution for thickness differentiation of the order of 4000Å at a frequency belt of around 20 KHz. The ability of generating this frequency is easier, and can be studied clearly. The pattern of distribution of group velocity is seen to diverge more at lower frequencies than at higher frequencies. In other words, the change in the slope of the different thickness lines for a particular frequency band is more at lower frequencies, which makes distinguishing easier. It can thus be suggested that lower frequencies be studied for thickness differentiation, and that in order to achieve better resolution (thinner layers), lower frequencies need to be examined.

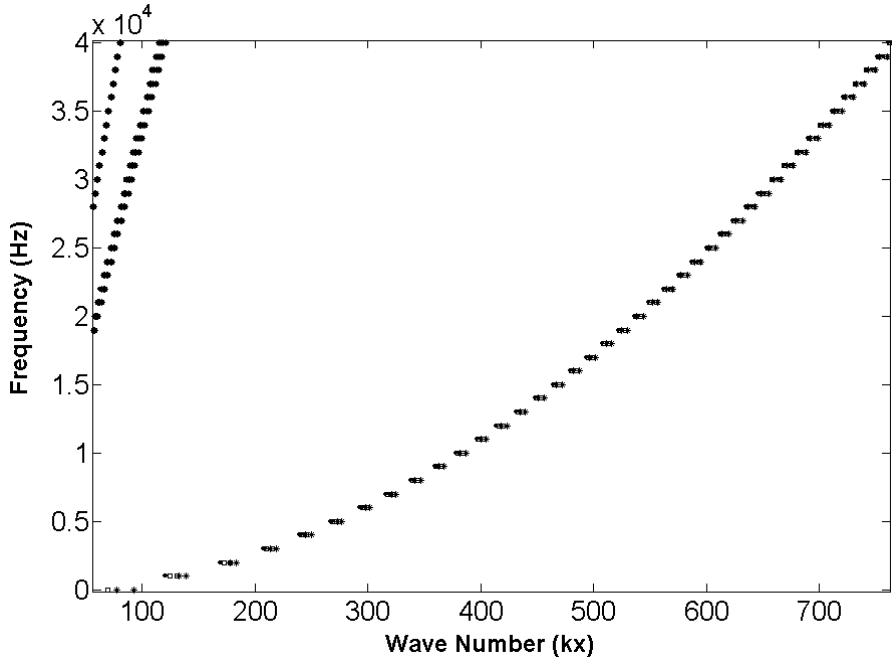

(a)

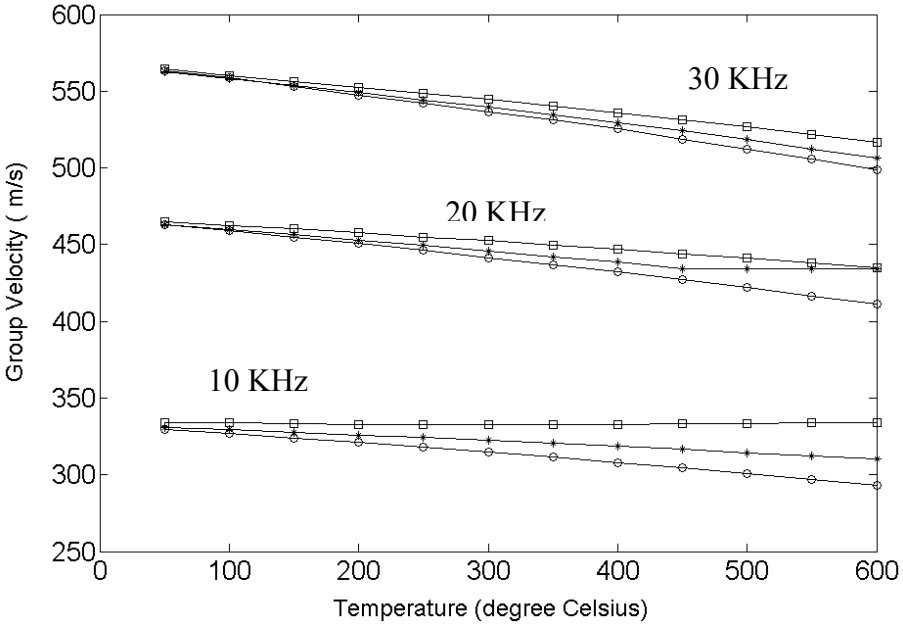

(b)

Figure 2-8 (a) Dispersion model showing convergence of thickness bands with increasing frequency, and (b) comparison of three lower frequency bands showing decreasing slopes of different thickness bands with higher frequencies (NOTE: legend for different thickness as shown in Figure 2-6)

CHAPTER III

EXPERIMENTAL SETUP AND PROCEDURES

A proper tool for semiconductor applications has to be a proven technique that can possibly gather information from the heated side of the wafer inside the RTP chamber. Any technique for measuring thickness or temperature changes must be validated to show that these parameters are being monitored on the processing side of the wafer. Moreover, the method should be unaffected by temperature, stoichiometry, or electromagnetic interference.

The sensitivity of acoustic waves to thickness and temperature changes has been established in the preceding chapters. The implementation of an optical technique that can measure the out-of-plane displacements resulting from the generation of an acoustic wave in the wafer would be the ideal solution to thickness gauging. A Lamb wave generated on one surface of the wafer would be able to run across and through the wafer, and reveal information of the nature and content of the segment of the wafer under study.

The current facility at Texas A&M University has a laser based ultrasound generation and sensing technique called Thermo-Acousto-Photonic Non-Destructive Evaluation (TAP-NDE) that can be used effectively to study Lamb wave behavior on silicon wafers with varying thickness, at varying temperature. The system uses optical fibers for sensing, and can be extended to remote sensing applications where a specimen such as the wafer has to be monitored on a real-time basis and continuous information has to be gathered.

LASER-BASED ULTRASOUND GENERATION

White [15] first suggested the generation of ultrasonic waves by short-pulse heating using lasers. A large amount of energy is sent into a focused point on the specimen by using a laser pulse.

The time duration of this pulse is normally in nanoseconds. Such an incident laser pulse results in a short-time increase of temperature at the point of incidence. The induced thermal energy is small enough to prevent any change in the solid state of the material. However, this energy is dissipated almost immediately as an elastic mechanical wave. As shown by Aussel et al [16], a low power density laser causes elastic stresses in the material resulting from bulk thermal expansion. Surface ablation is undesirable as it causes the rapid thermal expansion to shoot above the thermo elastic region, and causes melting, and hence vaporization of some of the material on the surface. This plasma creation effect is an irreversible occurrence, and the vaporization energy that is lost is not converted into a mechanical wave. Moreover, the thermal constants of the material are no longer a constant function of temperature, and the vaporization continues for a time instance beyond the pulsing duration.

However, with an incident laser pulse of low power density, the local increase in temperature at the point of impingement is adequately small to avoid any change of state. With a low incident power density, the material temperature is found to rapidly drop below its vaporization temperature after each pulse, and thus the normal stress is pulsed. For a high power density, the vaporization continues beyond the pulse duration. Thus, surface ablation due to laser irradiation is an effect that can possibly result in undesired stresses in the material. By ensuring that there was no surface ablation, the same wave pulse was generated repetitively in the wafer in this thesis volume.

Ultrasound generation in TAP-NDE is achieved with a Spectra-Physics model DCR-3 Nd: YAG laser with a pulse width of 10 nanoseconds. The maximum single pulse energy from the laser is 1 Joule. A 532-nm wavelength green light can be initiated from the laser using a harmonic frequency doubler, though the unaltered laser output wavelength is 1064-nm. The resulting beam is transmitted through an aperture to the surface of the specimen. A lens is used

for focusing the beam to the required spatial density before the beam converges on the surface. Care is taken to make sure that surface ablation is prevented to stick onto the elastic bounds of the generated acoustic wave. The thermal expansion at the point of contact and subsequent energy conversion results in an elastic Lamb wave that propagates radially outward.

The Nd: YAG laser was set to a output energy that was experimentally determined to be sufficient to generate a sufficiently strong elastic wave, while at the same time, not ablating the surface of the specimen. This was done by iteratively locating the ideal spot size of laser impingement, by adjusting the distance between the lens and the wafer disc, so that there occurs no ablation, and there is a clear Lamb wave seen on the oscilloscope. The output energy of the Nd:YAG laser was also varied in order to find the optimal condition of operation.

WAVE SENSING - FIBER TIP INTERFEROMETRY

Remote sensing is achieved by means of using optical techniques that continuously monitor out-of-plane displacements on the wafer surface caused by the propagating Lamb wave. Fiber Tip Interferometry (FTI) is a broadband wave sensing technique developed at Texas A&M University [17], that forms the wave detection system in the TAP-NDE setup as shown in Figure 3-1.

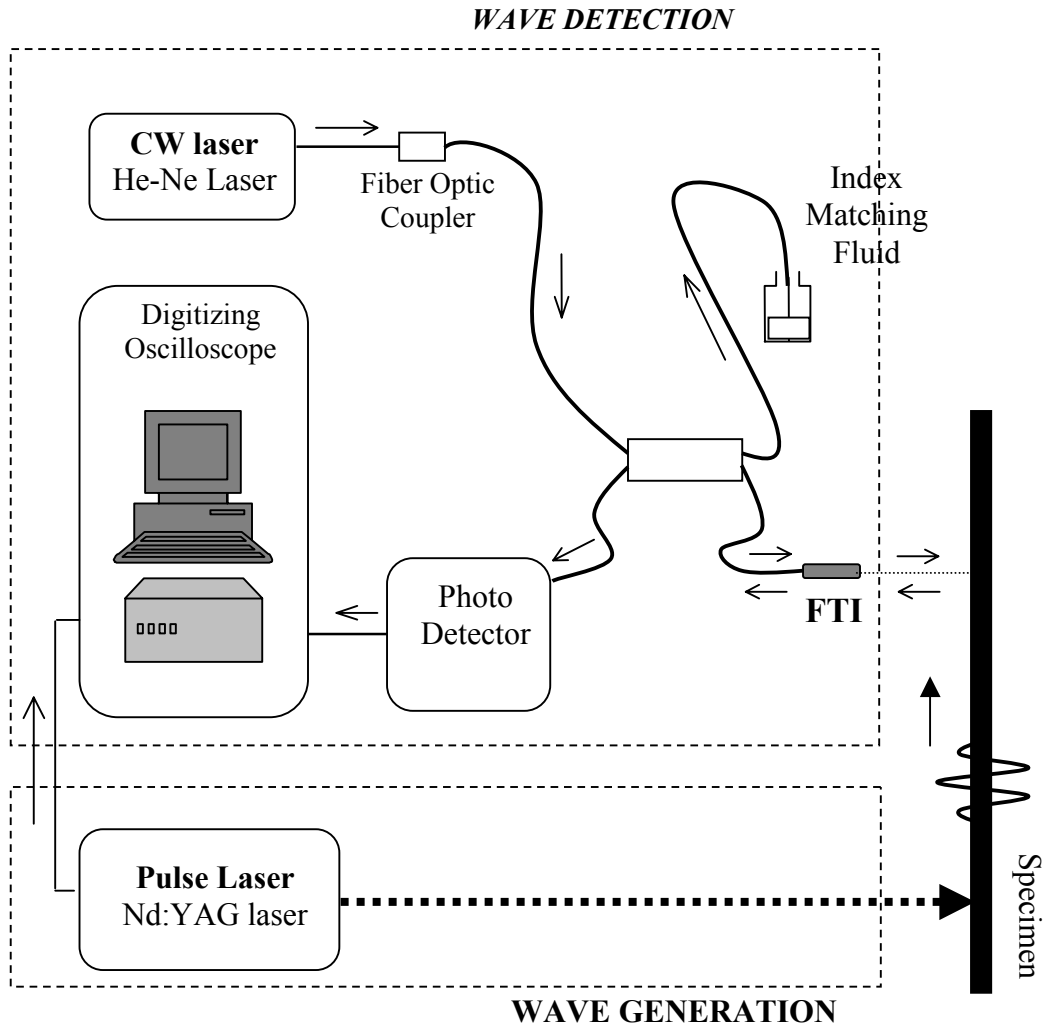

Figure 3-1 Schematic of TAP-NDE setup at Texas A&M University, College Station

FTI works on the basic Fizeau Interferometry principle, where the interference between a reference beam and the reflected beam is studied. Interference is observed when there is a constant phase shift between a coherent beam of light, and its reflected form. This occurs when the interfering beams originate from the same source, which can be achieved by using beam splitters. The particle displacements on the wafer surface caused by the traveling Lamb waves are significantly out-of-plane, as pointed out by Hutchins et al [5]. Out-of-plane displacements can be detected easily by interferometry and examined using time-frequency analysis techniques. In-plane displacements are much weaker, cannot be easily detected, and have no impact on the analysis techniques.

A schematic of the Fizeau principle and its extension to the FTI system is shown in Figure 3-2. The monochromatic light source in the FTI setup is a continuous wave He-Ne laser operating on the 632-nm red wavelength. The emitted beam is focused into a single mode optical fiber by using either an FC coupler, or a collimator lens setup. The fiber routes the beam to the specimen through a Fused Bi-conical Taper Coupler.

The tip of the fiber carries a GRIN lens that serves the purpose of back-reflecting a fraction of the coherent source of light. About 4% of the light from the laser is sent back into the fiber and forms the *reference beam* for the FTI. The remaining light gets reflected off the surface of the specimen and a portion of this re-enters the GRIN lens. This beam is called the *reflected beam*. There exists a constant phase change between the reference and the reflected beam, which gives rise to an interference pattern. The fused bi-conical coupler routes this interference beam to a photo-detector. This photo-detector converts the interference patterns into voltaic changes, and can operate up to frequencies as high as 25 MHz without hindrance from accompanying circuitry.

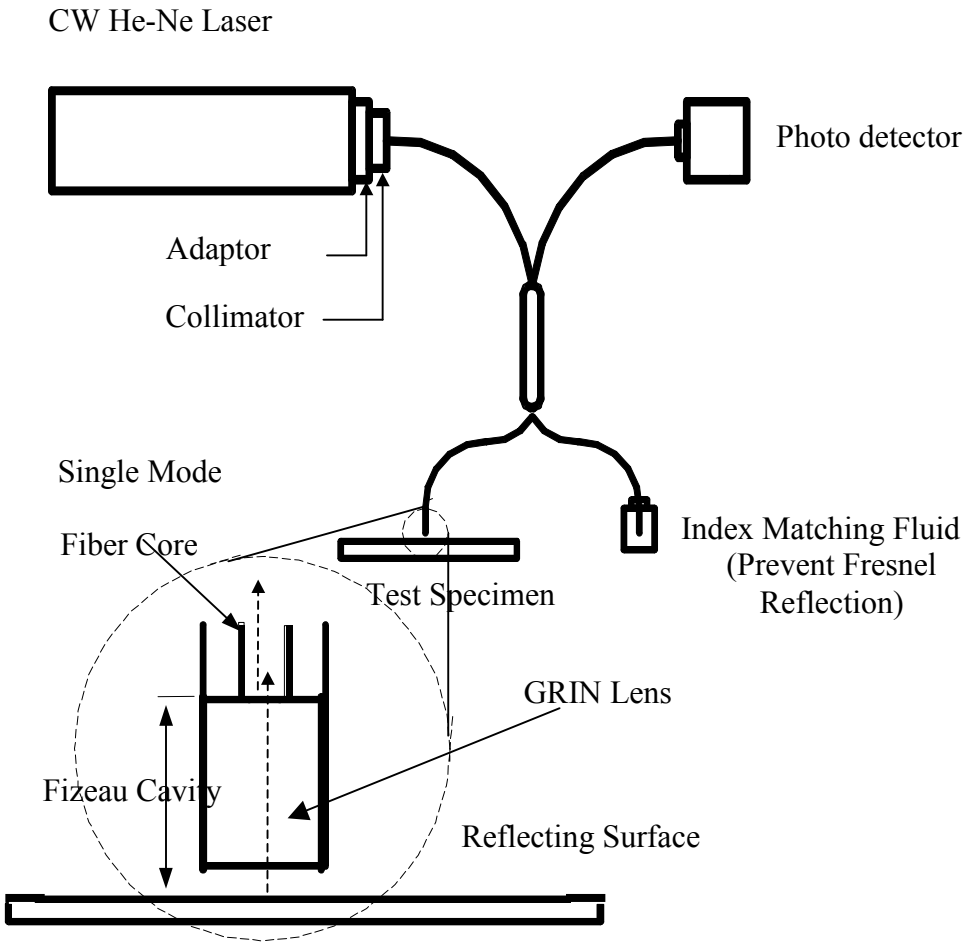

Figure 3-2 Wave detection system of TAP-NDE

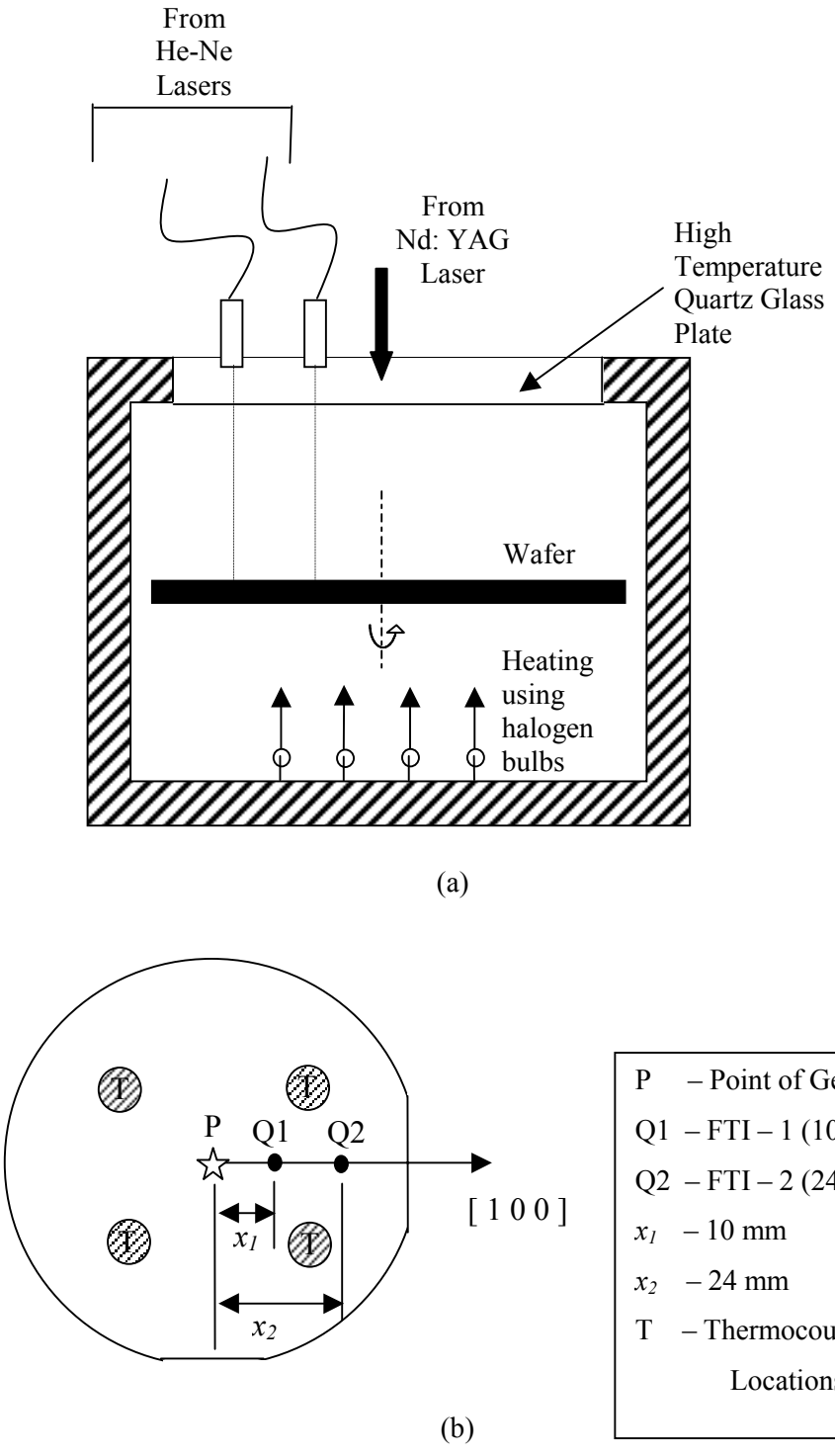

Figure 3-3 (a) Thermal chamber system with the dual FTI system incorporated – a sample model, and (b) wafer profile with generation, FTI and temperature study locations

The use of dual or multiple FTI systems on different regions of the wafer to analyze a single pulse would help record the behavior of a radially propagating Lamb wave. Such a setup is illustrated in Figure 3-3, which would help record data on a real time basis, as the wafer spins about its axis inside the rapid thermal-processing unit. The FTI setup described here is most ideal for data accumulation as it records unaltered, unaffected data originating from the wave, as against transducer-based techniques. In this thesis volume, a dual FTI system has been employed for measuring the out-of-plane displacements, as shown in Figure 3-3.

DATA ACQUISITION SYSTEM (DAS)

A Hewlett-Packard 5411D Digitizing Oscilloscope is used to record the waveform as sent by the photo-detector. The oscilloscope can be configured for sample rates up to 1 GHz per second. Each waveform is then digitally captured in binary form using a wave capture tool in Microsoft Excel, and the time-amplitude data is used for further analysis.

WAFER SAMPLES

A number of different wafers were acquired from Silicon Valley Microelectronics Inc. as part of research samples. The diameter of each wafer was 100±0.5 mm, and had a [100] orientation primary flat, and a secondary flat at a 90º angle. Pure silicon p-type wafers with Boron as dopant were used as the substrate wafer. The thickness of the substrate wafer was set at 525±25 microns.

Two sets of aluminum-coated wafers were obtained to characterize thickness change for an aluminum deposition layer. They were

- A plain Silicon wafer with the same dimensions as mentioned above, with a 250-angstroms coating of Titanium and a 4000-angstroms coating of Aluminum, and

- A similar plain Silicon wafer with a 250-angstroms coating of Titanium, and an 8000-angstroms coating of Aluminum on top of Titanium.

THERMAL CHAMBER SETUP

A thermal chamber was designed and fabricated in order to simulate the RTP environment as closely as possible at the laboratory level. The wafer was housed in the vertical position, so as to suit the existing laboratory setup of a horizontal pulsing beam from the Nd: YAG laser. The positioning of the wafer was achieved by the two flats on the flange surfaces that correspond to the ones on the wafers. A V-groove running around the flange surfaces helped to locate the wafer in the vertical position. A *quartz glass plate* was mounted on the front side of the system so as to accommodate wave generation and sensing, and at the same time, rendering the system as a closed unit. Such an arrangement can be overridden in commercial applications by suitable positioning of optic fibers that carry the beams.

The chamber carried a *water jacket* at the back end that formed the bulb housing system. *Double-ended halogen bulbs* placed linearly act as the heating elements. Appropriate ceramic insulation was provided to make the chamber electrically insulated. *Thermal insulation* using flexible ceramic sheets was also achieved on the inner surface of the *water jacket* so as to concentrate the radiated energy to the surface of the wafer. The bulbs were connected in parallel and a *variable resistor* was used to control the current flowing through them.

A simple water jacket system was also constructed using a concentric-tube heat exchanger principle. The outer pipe had two collars to provide the inlet and outlet for the water-based cooling system. Cool water flowed into the chamber through a low-pressure, low-volume electronic DC *fuel pump*, while the outlet collar sent the steam into a *transmission cooler* setup through a windshield *reservoir*. A schematic of the setup is shown in Figure 3-4.

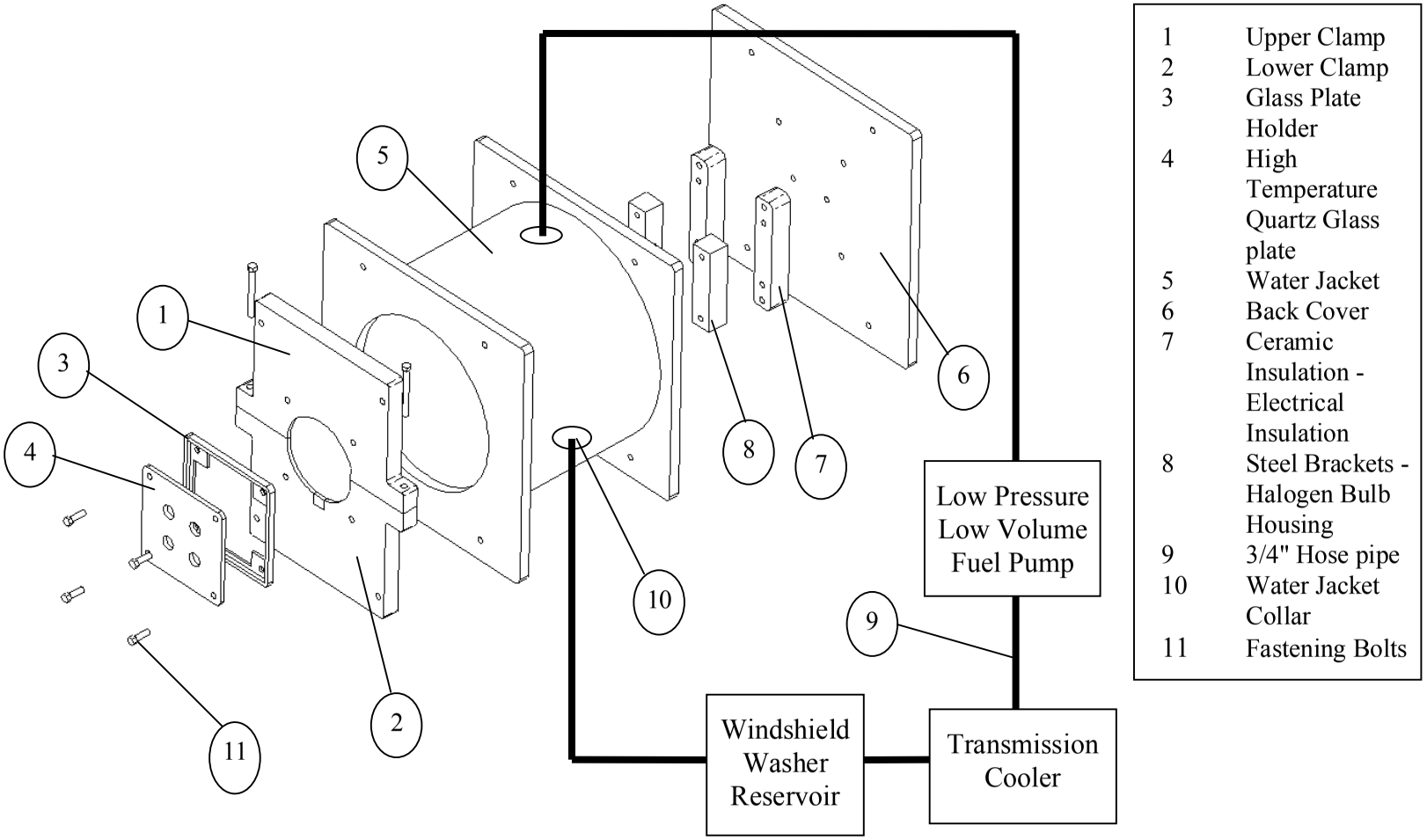

Figure 3-4 Thermal chamber setup designed for laboratory testing of wafers

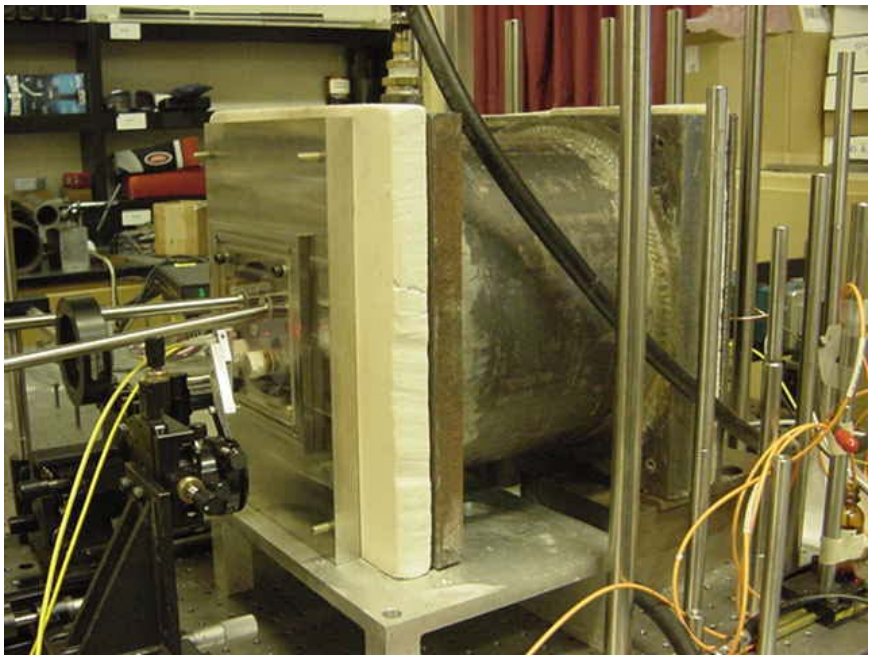

(a)

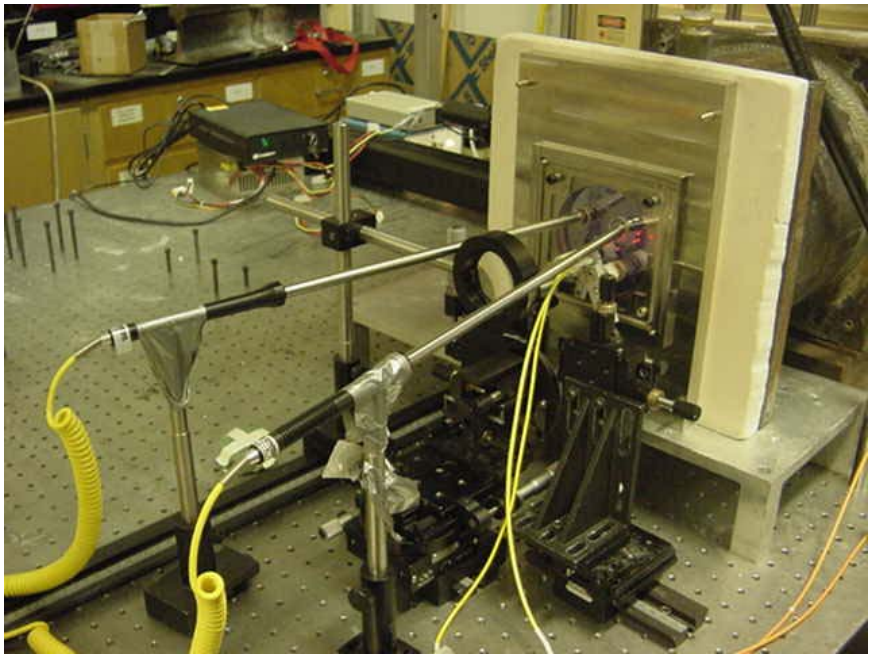

(b)

Figure 3-5 (a) Thermal chamber setup at the laboratory, and (b) Silicon wafer inside the chamber, with the FTI mountings, and the thermocouples in position

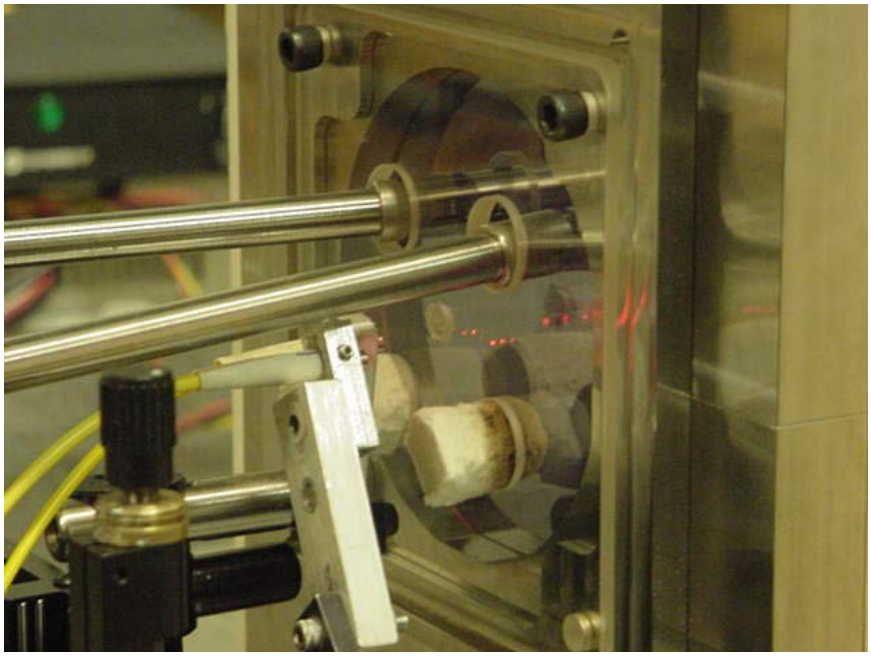

(a)

(b)

Figure 3-6 (a) Close-up of the silicon wafer mounting, with the FTI beams and the thermocouples in position and (b) a view of the windshield water reservoir mounting from the outlet of the water jacket, and the variable resistor to vary the voltage across the bulbs

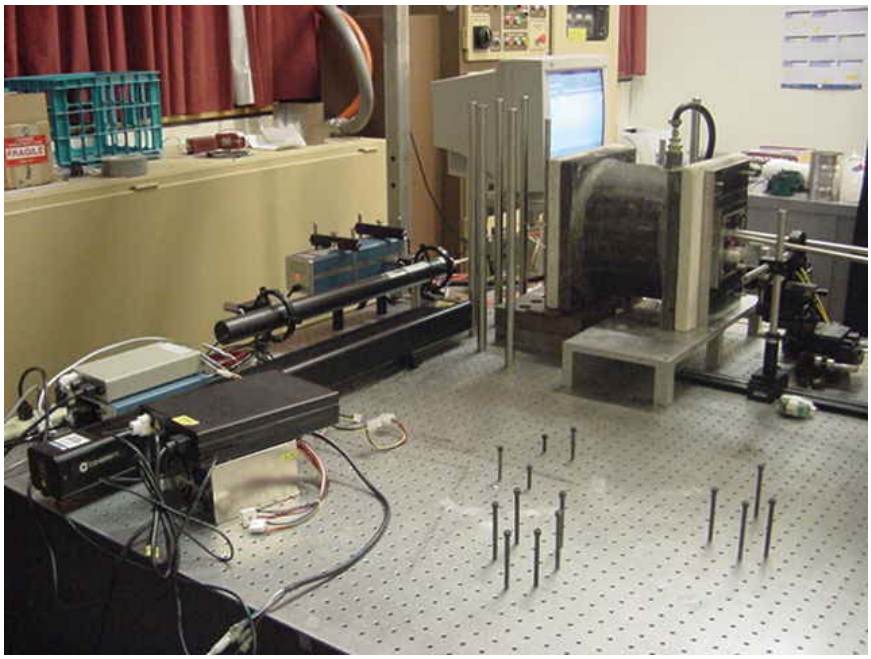

(a)

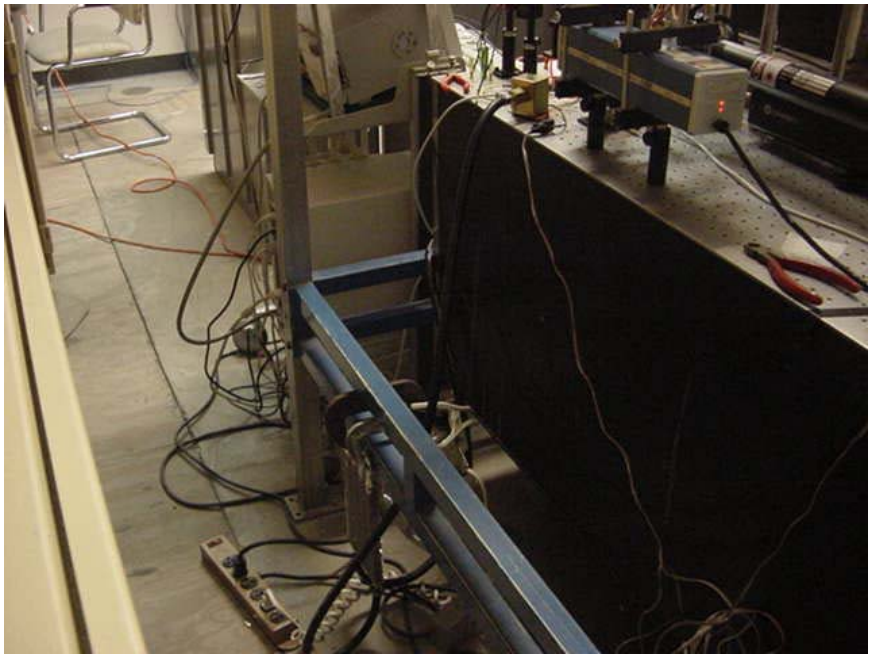

(b)

Figure 3-7 (a) He-Ne lasers at the laboratory, and (b) the location of the air cooled transmission cooler and the LP-LV fuel pump

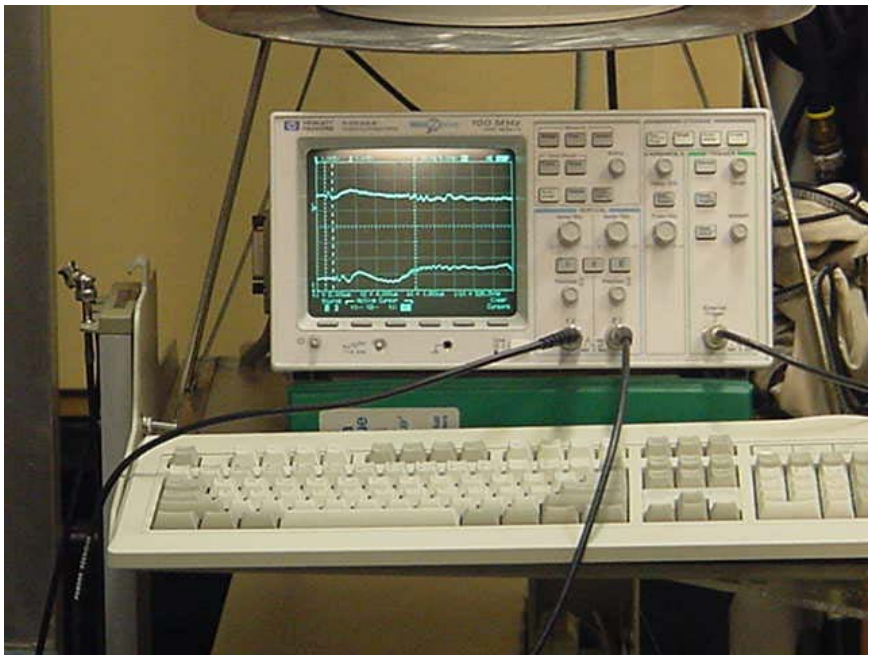

(a)

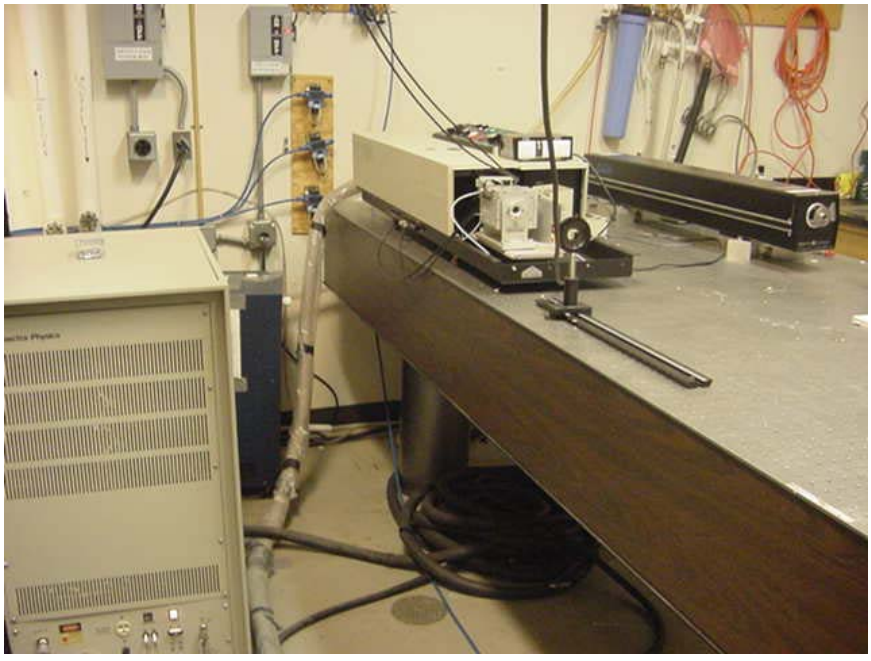

(b)

Figure 3-8 (a) Data acquisition through the oscilloscope, and (b) Nd:Yag laser setup at the laboratory

Figures 3-5 to Figure 3-8 show the realization of the illustrated design of the thermal chamber. The thermal chamber was used to mount the wafer in the vertical plane, with the heat exchanger system for steady state conditions, and the electrical circuit to generate heat through radiation from halogen lamps. The *clamps* helped to achieve a fixed orientation for the wafer, and the sensing beams from the GRIN lens were positioned along the [100] orientation. The setup also ensured that the pulsing beam repeatedly hit the same spot on the wafer to accomplish repeatability.

The quartz glass plate served the double purpose of permitting the laser beams to pass through to the wafer, while at the same time, providing an enclosure for the wafer to close the heating system, and thus insulate the wafer from room temperature. Two of the holes in the glass plate carried the *thermocouples* to measure the temperature on the surface of the wafer, while the free holes were plugged with insulation.

A variable resistor was used to control the flow of current across the halogen bulbs, and thus help in gradually heating the system to the desired temperature. Current continuity was ensured at all points from the bulbs to the variable resistor, while at the same time, ensuring discontinuity between the electrical circuit and the thermal chamber setup. A ground fault interrupt (GFI) was also used in the circuit so as to trip the circuit in case of accidental leakage of current.

EXPERIMENTAL PROCEDURE - TEMPERATURE RESOLUTION TESTS

The industry demands an accurate estimation of the temperature of the wafer at the test locations. The TAP-NDE technique needs to be proven to achieve a temperature resolution that is within the acceptable limits of industrial manufacturing requirements. In order to demonstrate this, the bare Silicon wafer was chosen as the test specimen.

Three tests were conducted on the wafer to determine the limits of resolution that can be achieved by TAP-NDE. Suh et. al [18] showed that TAP-NDE could display a resolution of up to ± 20 degrees Celsius. A part of the work done in this study was to demonstrate better resolution capabilities. All tests for resolution were demonstrated in the 200°C - 300°C temperature belt.

- The thermal chamber was used to mount the wafer such that the first FTI was at 10 millimeters from the point of generation (center of the wafer), and the second FTI was at 24 millimeters from the point of generation. The FTI systems were positioned such that maximum intensity of light was reflected back into the fibers after reflecting off the wafer surface.
- The Nd:YAG laser was used to trigger a thermo-elastic wave through the wafer. The out-of-plane displacements resulting from the propagating wave was captured by the FTI systems as phase changes between the reference and the reflected beams. The corresponding voltaic changes were captured on an oscilloscope, and then on a time-versus-amplitude data format using a data capture tool in Microsoft Excel.
- Temperature was increased from room temperature to 200°C, by adjusting the variable resistor to allow the necessary amount of current through the halogen bulbs. The temperature was read off the thermocouples that were periodically made in contact with the wafer surface. Upon observing the stabilized temperature, the thermocouples were withdrawn, and a thermo-elastic wave was triggered again through the wafer. The Lamb wave that was generated was captured as described earlier.
- In order to estimate the ±10°C resolution of the system, temperature was then increased to 210°C, and then the same procedure as described above was repeated in order to

capture the corresponding Lamb wave data. Such readings were taken periodically in steps of 10°C up till 270°C.

- For a ±5°C resolution, the temperature was incremented from 270°C to 300°C in steps of five degrees Celsius. The same procedure of using the Nd:YAG pulse to generate a wave, and sense using the FTI system was utilized to record the Lamb wave data.
- The ±1°C resolution tests were conducted on a similar basis from 290°C to 300°C, and the corresponding data was recorded.

EXPERIMENTAL PROCEDURE - THICKNESS DIFFERENTIATION TESTS

The objective of these tests were to determine the feasibility of TAP-NDE towards resolving the difference between a plain wafer substrate, and a wafer of arbitrary thickness, so as to demonstrate the ability to differentiate between regions of different thickness on a real-time basis during processing [19]. The following steps were involved in differentiating between wafers of different thickness:

- The plain wafer, with Silicon substrate, was interrogated using the TAP-NDE setup for a temperature range of up to 600°C in steps of 50°C. The corresponding Lamb wave data was captured from the oscilloscope as time-amplitude information by using the wave capture tool in Microsoft Excel.
- The wafer with 4000°A of Aluminum and 8000°A of Aluminum were interrogated using the same technique for the same temperature steps as that of the plain wafer and the data were recorded in a similar fashion.

CHAPTER IV

FEATURE EXTRACTION TECHNIQUES

Acoustic signal processing is an essential ingredient in the characterization of acquired data. A typical waveform that is obtained in the time domain does not provide sufficient basis for comparison with other similar waveforms. The propagating wave is essentially a multi-frequency signal, whose spectral information is concealed in the time domain. In such instances, transformations gain much value as they help in providing a different, more compatible and easier form of signal comparison [20].

FOURIER TRANSFORM

Linear transforms find diverse applications in systems analysis, modeling, boundary value problems and scientific disciplines. The Fourier Transform has become one of the widely accepted versatile tools for mathematical and scientific analyses, by transforming a time-amplitude domain waveform into the frequency-amplitude domain.

$$X(f) = \int_{-\infty}^{\infty} x(t)\, e^{-i\omega t}\, dt \qquad (4-1)$$

In mathematical terms, an unknown waveform or function can be decomposed into an infinite sum of periodic complex exponential functions that are of different frequencies. It can be seen from the above equation that Fourier transform is achieved by taking an inner product of the unknown function with a set or a bank of exponential functions.

If, for a particular exponential function frequency, the integration results in a high magnitude vector, then the presence of that frequency component in the signal is high. Similarly, the relatively low magnitude vector resulting from the above integration denotes the

small amplitude of that frequency component. If the output is a zero vector, then that frequency is absent in the waveform being examined. The discrete form of FT is used for computer simulations of the continuous signal, and is given by

$$X(k) = \sum_{n=0}^{N-1} x(n)\, e^{-i\,2\pi\, n k / N} \qquad (4-2)$$

The Fourier transform gives a clear indication of the presence of the frequency components in the signal irrespective of the time at which the component appears. If a frequency component is within the bounds of the chosen exponential functions, then the frequency vector is seen in the DFT irrespective of its arrival time. This inhibits the application of DFT towards the analysis of non-stationary signals, where frequency is found to vary with time.

SHORT TERM FOURIER TRANSFORM

The use of the Short Term Fourier Transform (STFT), also known as the windowed Fourier Transform, is a step towards compensating for this problem. A non-stationary signal can be broken into segments, or windows, where the signal can safely be assumed to be stationary. The width of the window should be narrower than the width of the stationary portions. Convolution of the window function with the original signal gives the segment of the signal enveloped by the window.

$$STFT(b,a) = \int_{-\infty}^{\infty} f(t)[\phi(t-b)e^{-iwt}]\,dt \qquad (4-3)$$

A normal DFT of such a function would give the spectral information on a time-frequency representation, limited by the width of the window. The window is then translated along time so as to examine the entire length of the signal. Such a translation results in a joint

time-frequency representation of the waveform. An ideal windowing function would analyze the signal at every instance of time, and for the shortest intervals of time, without actually overlapping with each other. Such a window would be an impulse function. However, it is impossible in discrete mathematics to actually analyze all intermediate sections of the unknown signal if an impulse function is used as the window. The closest approximation to an impulse function would be the Gaussian function, which is given by

$$\phi(t-b) = e^{\frac{-a}{2}(t-b)^2} \qquad (4-4)$$

An important feature of the STFT is the width of the window that is used. A narrow window would give better time resolution, but poor frequency resolution, and vice versa. For a fixed window, the time and frequency resolution at all instants of the waveform is fixed. This trade-off between time and frequency resolution is a critical limitation in joint time-frequency analysis, and is explained by the Heisenberg Uncertainty Principle.

$$Time - Bandwidth\ \mathrm{Pr}oduct = \Delta t\,\Delta f \geq \frac{1}{4\pi} \qquad (4-5)$$

This principle was originally used to prove the uncertainty in simultaneously pinpointing the location and momentum of a moving particle. When extended to time-frequency representation, it can be shown that the time and frequency resolution are limited by the lower bound of their product, given by the above equation.

STFT can thus be seen to be a successor to traditional Fourier representations of the signal, but is limited in terms of resolution. Wavelet transforms address these pitfalls and hence prove to be a more sophisticated tool for mechanical signature analysis.

WAVELET TRANSFORM

The foundations of the modern wavelet based approach date back to the early eighteenth century, but their applications have gained significant importance in the past two decades. Wavelet transforms (WT) consist of a family of representations using hierarchical orthogonal basis functions. Contrary to STFT, where a fixed window width is used for analysis, WT employs a wavelet that continuously varies in scale.

As seen in the Heisenberg uncertainty principle, resolution is limited at best to a certain level, beyond which it is impossible to clearly pinpoint the arrival of a particular frequency. WT is superior in this aspect when compared to STFT, due to its ability to scale the window so as to examine higher frequencies with a compressed window, and lower frequencies with a dilated window.

The concept of WT is better perceived in terms of filter banks as consisting of a set of constant Q- band pass filters. The bandwidth of a particular spectrum is defined as the difference between the higher and lower cut-off frequencies. The Q of a band pass filter is a measure of the ratio of the central frequency to its bandwidth, and is given by

$$\frac{\Delta f}{f} = c \qquad (4-6)$$

For a constant Q filter, the bandwidth varies as a function of its center frequency, always keeping the ratio between them the same.

The Continuous Wavelet Transform (CWT) is based upon the above ideas, and is defined as

$$WT_{a,b} = \int_{-\infty}^{\infty} f(t) \cdot \overline{\psi_{a,b}(t)}\, dt \qquad (4-7)$$

It should be noted that the impulse response of all the analysis filters in the filter bank can be seen to be scaled versions of the mother wavelet, that is, the traveling wavelet is stretched or compressed, based upon a scale factor *a*, so that

$$\psi_{a,b}(t) = a^{\frac{-1}{2}} \psi(\frac{t-b}{a}) \qquad (4-8)$$

In this case, the frequency response of the analysis filter will have its central frequency at $f = f_o / a$. It can thus be seen that the local frequency is no longer a function of frequency modulation, but is a function of the scaling parameter, *a*.

Scaling and translation are two important parameters that govern the movement of the analyzing wavelet across the unknown signal. Translation corresponds to the time information in the transform domain. The parameter *b* as seen in the wavelet function is the translation parameter, and dictates the travel of the wavelet along the time axis.

Scaling corresponds to the compression or dilation of the wavelet. In general terms, smaller scales refer to a more dilated view of the system. However, since the scaling parameter appears in the denominator of the wavelet function, for each incremental value of the scale parameter *a*, the wavelet is seen to dilate. Scale and frequency correlate with each other such that lower scales correspond to higher frequencies, and vice versa. The frequency resolution that is achieved is determined by the width of the time window.

An analyzing function is a suitable mother wavelet if it satisfies two admissibility conditions. First, the reconstruction condition is

$$\int \psi(t) dt = 0 \qquad (4-9)$$

which implies that the area bounded inside the wavelet is zero. Secondly, the analyzing wavelet should be of finite energy, which is ensured by selecting the wavelet function such that the function and its Fourier Transform satisfy

$$\int_{-\infty}^{\infty} \left| t\psi(t) \right|^2 dt < \infty \qquad (4-10)$$

$$\int_{-\infty}^{\infty} \left| \omega\hat{\psi}(\omega) \right|^2 d\omega < \infty \qquad (4-11)$$

In accordance with the sampling theorem, a narrow window is required to detect high frequencies, and a sufficiently wide window is necessary to study low frequencies. The scaling parameter in the wavelet transform helps to automatically satisfy this requirement since the width of the time window is proportional to the scaling parameter, that is, inversely proportional to the frequency. This characteristic enables the wavelet transform to study a wide range of frequencies. This overrules the STFT limitation where the resolution needs to be adjusted to suit the window width.

THE GABOR WAVELET TRANSFORM

The Gabor wavelet, shown in Figure 4-1, has been adopted as the analyzing mother wavelet because of its smaller area of time-frequency window when compared to any other function. The Gabor function is a complex planar function restricted by a two-dimensional Gaussian envelope. These Gaussian modulated complex exponentials were shown to give the best trade off between time and frequency resolution. The Gabor wavelet permits local frequency information at each location in the image and is thus a common tool in image analysis.

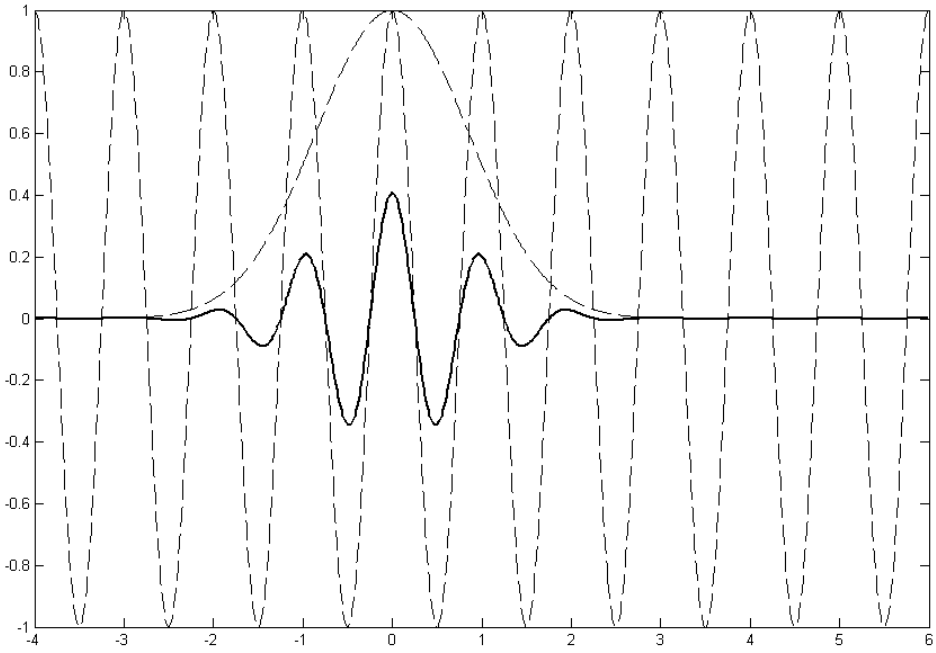

(a)

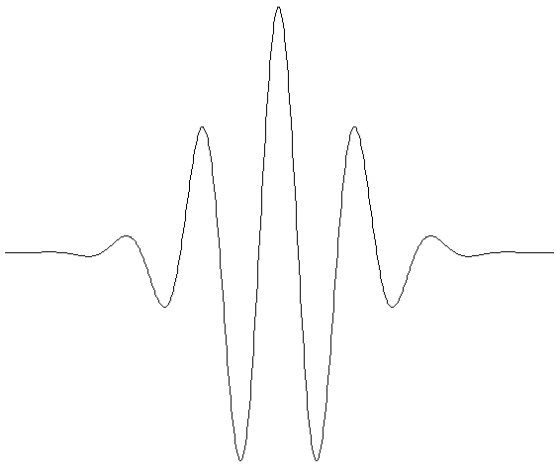

(b)

Figure 4-1 (a) Gabor function as a convolution of a complex sinusoid and a Gaussian, and (b) the Gabor wavelet

A typical two-dimensional Gabor wavelet formulation can be seen to be the convolution of two orthogonal components, that is, a Gaussian, and a complex sinusoid, and is defined by,

$$\psi_s(t) = \frac{1}{\sqrt[4]{\pi}}\sqrt{\frac{\omega_0}{\gamma}}\exp\left[-\frac{(\omega_0/\gamma)^2}{2}t^2 + i\omega_0 t\right] \qquad (4-12)$$

The Gaussian part of the Gabor function is centered at the origin, while the Fourier transform is a Gaussian curve centered at f_o. If the value of γ is maintained sufficiently large, the Gabor function can be seen to satisfy the admissibility condition. For the analysis in this thesis, γ was found to give a sufficient resolution of the time-frequency plot if it was set at 600.

TIME-FREQUENCY ANALYSIS OF WAVE PROPAGATION

It is important to understand the application of wavelet-based analysis in understanding wave propagation, in order to perceive the physical meaning of time-frequency representation of waveforms. In the case of propagating a Lamb wave through Silicon using TAP-NDE, the method of generation is broadband, that is, many different frequencies are simultaneously generated. During such a case, the feature extraction tool effectively distinguishes one frequency component from another in a time-frequency analysis of the waveform. Such an analysis where distinguishing between the different frequency components is clearly presented in the study by Kishimoto et al [7]. The authors have described a simple means of understanding the concept of time frequency analysis when applied to wave propagation, which will be discussed in this section to familiarize the concept of time frequency analysis of a propagating wave.

Consider the propagation of a wave with two frequencies ω_1 and ω_2 defined by the equation

$$u(x,t) = e^{-i(k_1 x - \omega_1 t)} + e^{-i(k_2 x - \omega_2 t)} \qquad (4-13)$$

along the x-axis. The above equation can be re-arranged to give

$$u(x,t) = 2\cos(\Delta kx - \omega t)e^{-i(k_c x - \omega_c t)} \qquad (4-14)$$

where

$$k_c = \frac{(k_1 + k_2)}{2}, \omega_c = \frac{(\omega_1 + \omega_2)}{2} \qquad (4-15)$$

$$\Delta k = \frac{(k_1 - k_2)}{2}, \Delta\omega = \frac{(\omega_1 - \omega_2)}{2} \qquad (4-16)$$

The wavelet transform of the function *u(x,t)* is given by

$$WT_{x,a,b} = \sqrt{a}\left[e^{-i(k_1 - \omega_1 b)}\overline{\hat{\psi}(a\omega_1)} + e^{-i(k_2 x - \omega_2 b)}\overline{\hat{\psi}(a\omega_2)}\right] \qquad (4-17)$$

Upon taking the magnitude,

$$\left|WT_{x,a,b}\right| = \sqrt{a}\left\{\begin{matrix}\left[\hat{\psi}(a\omega_1)\right]^2 + \left[\hat{\psi}(a\omega_2)\right]^2 \\ + 2\hat{\psi}(a\omega_1)\hat{\psi}(a\omega_2)\cos(2\Delta kx - 2\Delta\omega b)\end{matrix}\right\}^{\frac{1}{2}} \qquad (4-18)$$

Two general cases can be inferred out of the above equation

- *Sufficiently small Δω* - In such a case, the wave has phase velocity $c_p = \omega_c / k_c$, and group velocity $c_g = \Delta\omega / \Delta k$. In this case, the Fourier transform of the scaled wavelet functions for the different frequencies ω_1 and ω_2 can be approximated to be equal to ω_c. Thus,

$$\hat{\psi}(a\omega_1) \approx \hat{\psi}(a\omega_2) \approx \hat{\psi}(a\omega_c) \qquad (4-19)$$

  And the magnitude becomes

$$\left|WT_{x,a,b}\right| \approx \sqrt{2a}\left|\hat{\psi}(a\omega_c)\right|\left[1 + \cos(2\Delta kx - 2\Delta\omega b)\right]^{\frac{1}{2}} \qquad (4-20)$$

  Here, the magnitude of the wavelet transform reveals a peak at $a = \omega_o / \omega_c$, and $b = (\Delta k / \Delta\omega)x = x / c_g$, which corresponds to the propagating wave.

- *Sufficiently large Δω* - Here, the Gabor function is localized around $\omega = \omega_o / a$, and if $\Delta\omega$ is large enough so that

$$\hat{\psi}_g(a\omega_1) \approx \hat{\psi}_g(a\omega_2) \approx 0 \qquad (4-21)$$

The magnitude thus becomes

$$\left|WT_{x,a,b}\right| \approx \sqrt{a}\left\{\left[\hat{\psi}(a\omega_1)\right]^2\left[\hat{\psi}(a\omega_1)\right]^2\right\}^{\frac{1}{2}} \qquad (4-22)$$

Since the magnitude reveals the presence of both frequencies, the wavelet transform would show two peaks, one at $a = \omega_o / \omega_1$, and the other at $a = \omega_o / \omega_2$, regardless of the value of *b*. It is thus seen that the ability to distinguish between two different peaks on the resulting time-frequency analysis is largely dependent on the difference in frequency, $\Delta\omega$. The ability of the wavelet to differentiate between the wavelet co-efficient of one frequency and that of another is dependent upon the scaling parameter, and on the sampling rate of the signal.

Depending upon how coarse or rough the number of steps of the scaling parameter is, the ability of the transform to distinguish between two different frequencies is determined. That is, for a rough, or coarse resolution, the differentiation is limited to a larger$\Delta\omega$, which would give two different values for the wavelet co-efficient. However, with a finer step, a small change in $\Delta\omega$ is spotted by the traveling wavelet.

Similarly, depending upon the sampling rate, the frequency range is determined, which once again influences the ability to distinguish between two closely located frequency components. The lesser the sampling rate, the lesser is the ability of the wavelet to distinguish between two closely located frequency components. During data acquisition, it is important to have a high sampling rate (set at 200 MSa per second on the oscilloscope for the experiments carried out in this thesis).

CHAPTER V

EXPERIMENTAL RESULTS

Tests for temperature resolution and thickness differentiation were performed as described in Chapter III. The data that was captured on the oscilloscope was found to satisfy the initial visual perception of the generation of a Lamb wave. However, at different temperatures, the changes in group velocity were so minimal that they could not be differentiated at a first glance.

TEMPERATURE RESOLUTION RESULTS

As seen in Figure 5-1, which shows the obtained waveforms on the oscilloscope for FTI-1 and FTI-2, the initial waveforms did not provide the desired differentiation for the application. The data that was recorded at a distance of 24 mm (FTI-2) from the point of generation was used to explain the temperature resolution issue.

The time-amplitude data was converted to time-frequency data by using the Gabor wavelet transform in the code written in MATLAB [Appendix - D] for the transformation. The input parameters in the code included the scaling function, the time step involved, and the Gamma function value desired for the analysis. In this case, the scaling step and the time step were 300 steps, and the gamma value was 600. The code output contained the GWT plots and the group velocity of the frequency coefficient maxima for each frequency step. A typical time-frequency plot is shown in Figure 5-2 (a), from which the arrival of each frequency coefficient was isolated. This extrema of frequency coefficients reflected on the arrival time of each of the frequency components of the propagating Lamb wave.

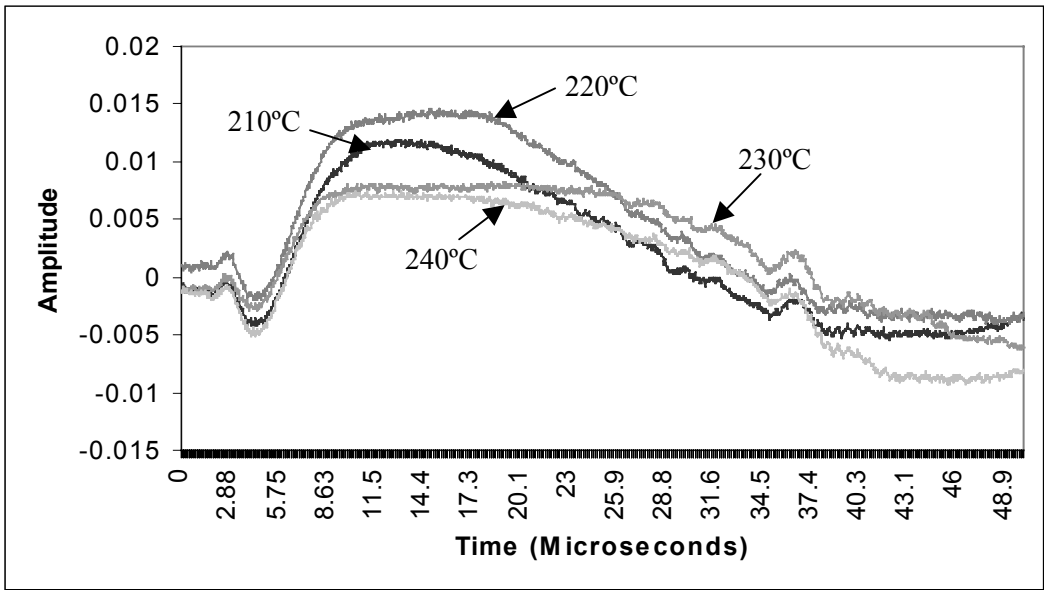

(a)

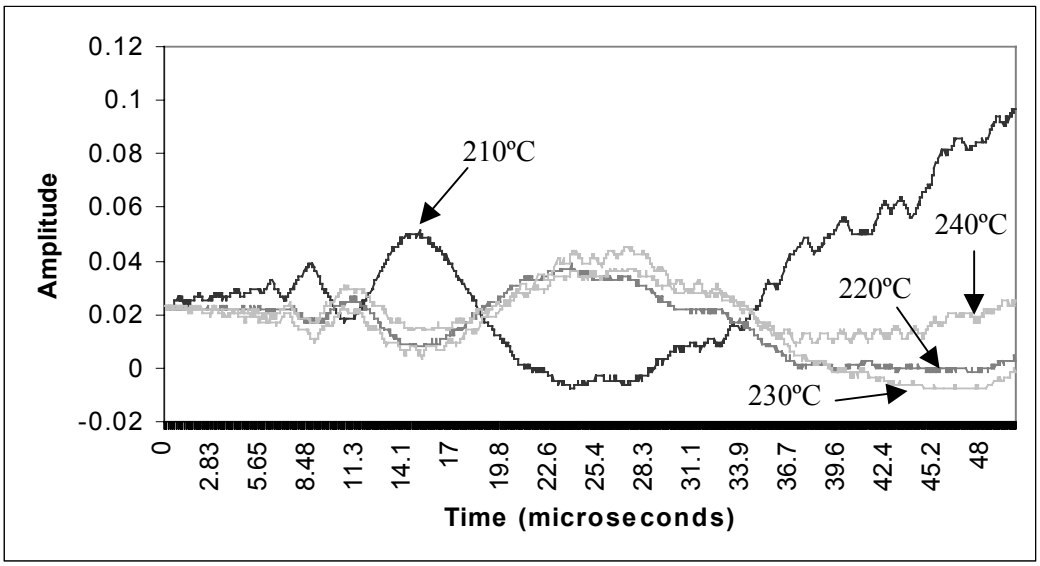

(b)

Figure 5-1 Data waveforms of (a) FTI –1, at a distance of 10 mm, and (b) FTI –2 at a distance of 24 mm, both captured from the oscilloscope display using Microsoft Excel

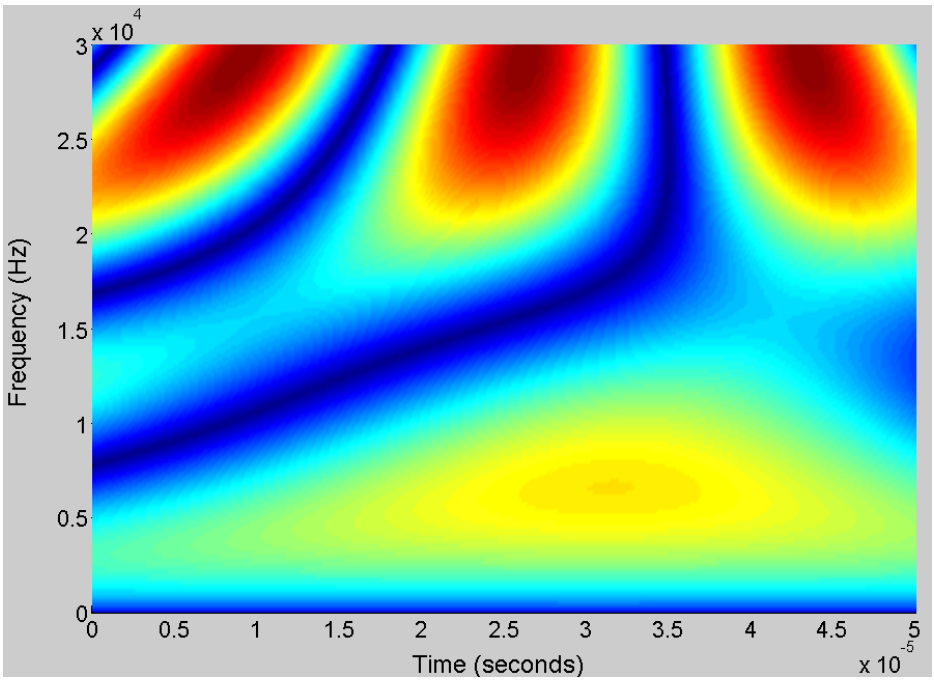

(a)

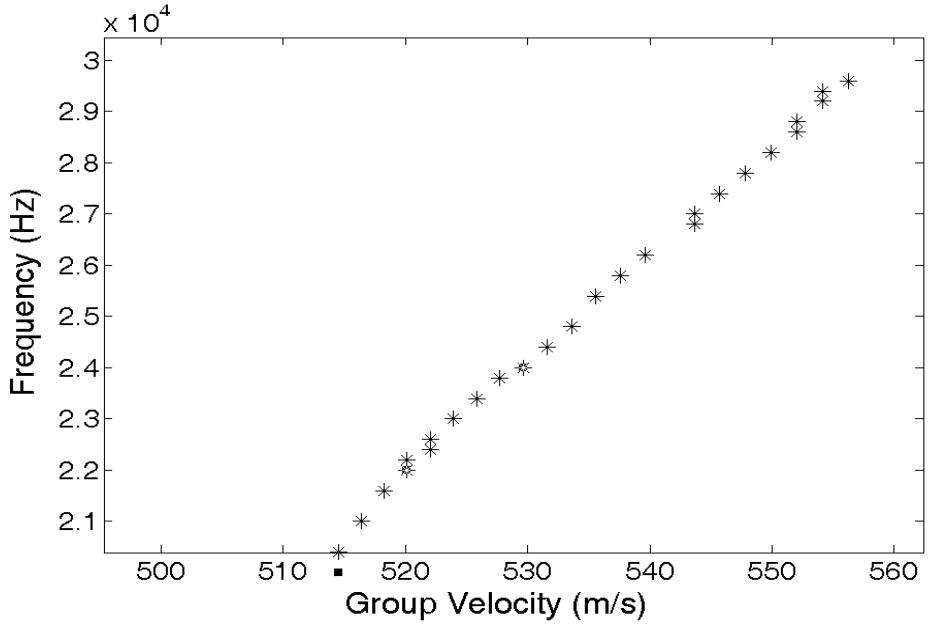

(b)

Figure 5-2 (a) Time-frequency plot from Gabor wavelet transform, and (b) the corresponding group velocity plot showing the group velocity of 23 KHz frequency (210ºC)

The group velocity of the required frequency component was determined by calculating the ratio of the distance traveled by the wave to the time of arrival of that frequency component. The 23 KHz frequency was selected for studying the resolution and thickness differentiation properties based upon the theoretical prediction model. This frequency is optimal for study, as it lay in a zone of compromise in resolution between temperature and thickness when studied as a function of group velocity.

A sample group velocity plot that was obtained at FTI - 2 is shown in Figure 5-2 (b). The 23 KHz frequency component was seen to have a group velocity of 524.5 m/s. In a similar fashion, the group velocity of the 23 KHz component was examined for different temperatures, from 200ºC to 270ºC, in increments of 10ºC. It is important to mention at this stage, that during experimentation, the spot size (determined by adjusting the distance from the focal lens to the wafer) was of a diameter of 2.5 mm. Such a spot size was found to enable the use of higher energy input without ablating the surface of the wafer. If the spot size were a point, the input energy used in experimentation would have ablated the surface of the wafer, as was experimentally determined by repeatedly adjusting the focal lens distance from the wafer.

Upon observing the group velocity plots for the ±10°C resolution data, it was seen that there was a negative slope of the growth pattern, as the temperature increases. This is in accordance with the theoretical group velocity prediction model. However, it was observed that though there was a match in the trend of the group velocity, the overall experimental velocity was about 45 m/s faster than that predicted by theory. This can be seen as illustrated in Figure 5-3, as a comparison between theory and experiment.

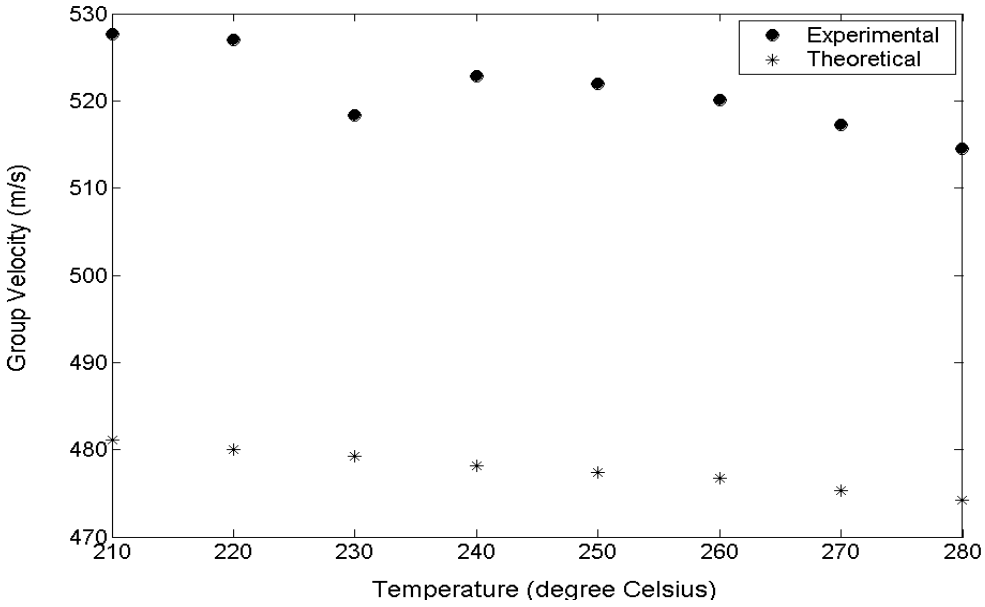

(a)

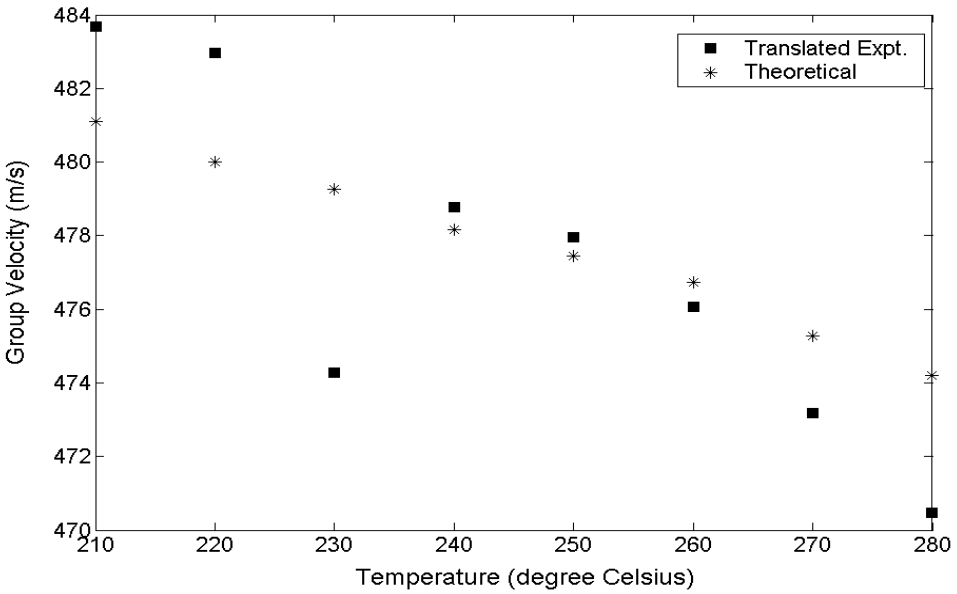

(b)

Figure 5-3 (a) Experimental versus theoretical group velocity for 23 KHz frequency for ±10°C resolution, and (b) translated experimental group velocity as compared to theoretical group velocity

There exist a number of reasons that can account for this shift in the experimental group velocity pattern. The contributing factors towards this shift in group velocity was analyzed, and the following was summarized from this observation:

- The shift could have been caused by parallax error during reading the distance between generation and sensing. Assuming this to be the only reason, it was found that if the reading had been 22.5 mm, the experimental group velocity is in good agreement with the theoretical values (Figure 5-3 (b)). This uncertainty in distance measurement of approximately ±1.5 mm was determined because of the spot size that was used, as explained earlier. The point of sensing was located easily, because of the sharpness of the point on the wafer from the GRIN lens. However, the spot size for generation, which was of a diameter of 2.5 mm, was large enough to allow for an uncertainty in measuring the exact distance from generation to sensing. The maximum concentration of the input energy was thus approximated to anywhere inside the spot, and thus accounts for the uncertainty in the distance between the points of generation and sensing.
- The read-off in the vernier calipers could also be a possible source of this difference in theoretical and experimental group velocities. The vernier calipers had a read-off of up to two significant digits, which could also influence the group velocity.
- Another possible error is the fact that, while it is desired and attempted to perform a study on the [100] axial orientation, angular alignment errors, which are also contributed due to visual observations, could account for a small change in the angular positioning of the FTI systems. In other words, if the point of generation, and the two points of sensing were all not on the [100] axial orientation, then the resulting group velocity is bound to change. The main reason for this is because Silicon has an orthotropic crystal axis orientation, because of which the stiffness across the wafer changes with the axis

orientation. Hence, the group velocity, which is a function of stiffness, is found to change. Under laboratory conditions, the accuracy of this positioning was limited by the ability of the human eye.

- Group velocity is seen to decrease in a very gradual fashion with increasing temperature. There is a drop of 10 m/s for every 50ºC rise in temperature. The thermocouples that were used in this study had an inherent drift of ±2.2ºC, which could also account for small changes in the group velocity.

The difference in theoretical and experimental group velocities can thus be explained by the above-mentioned causes for uncertainty. It is to be noted that these causes can be minimized and even excluded by a custom-based design to suit the end product requirement. By accounting for this difference in theoretical and experimental group velocities, it was seen that the experimental value had a very close agreement with the theoretically predicted values. The range of uncertainty is determined as shown in Table. 5-1 for predicting the accuracy of the experimental setup, as versus the theoretically predicted model. Table. 5-1 shows the determination of the range of uncertainty in percentage for a 10ºC resolution on the wafer.

Table 5-1 Group velocity translation and range of uncertainty calculation for ±10ºC resolution of the 23 KHz component

Temp (°C)	Expt. Group Velocity (m/s)	Theo. Group Velocity (m/s)	$GV_e - GV_{th}$ (m/s)	Average Diff. (m/s)	New Expt. Group Velocity (m/s)	Range of Uncertainty	Percent
200	529.3	482.21	47.09	44.03	485.27	0.006345783	0.635
210	527.7	481.1	46.6	44.03	483.67	0.005341925	0.534
220	527	479.99	47.01	44.03	482.97	0.006208463	0.621
230	518.3	479.26	39.04	44.03	474.27	-0.010411885	1.041
240	522.8	478.17	44.63	44.03	478.77	0.001254784	0.125
250	522	477.44	44.56	44.03	477.97	0.001110087	0.111
260	520.1	476.72	43.38	44.03	476.07	-0.001363484	0.136
270	517.2	475.28	41.92	44.03	473.17	-0.004439488	0.444
280	514.5	474.19	40.31	44.03	470.47	-0.007844957	0.784
290	519	473.35	45.65	44.03	474.97	0.003422415	0.342
300	516.7	472.52	44.18	44.03	472.67	0.000317447	0.032

The following relation gives the range of uncertainty,

$$Uncertainity_{(f)} = \frac{x_2 - x_1}{x_1} \qquad (5-1)$$

where x_1 is the theoretically predicted group velocity, x_2 is the experimentally determined group velocity, and f is the frequency band at which the study is based.

It was found that for the ±10°C resolution, the percentage range of uncertainty with which the TAP-NDE setup could resolve the change in group velocity with temperature was 0.43%.

A similar study was adopted for assessing TAP-NDE towards resolving ±5ºC. It was seen that there was a deviation in the experimental group velocity, when compared to the theoretical group velocity. This deviation was akin to that observed in the case of ±10ºC resolution tests. The possible causes for this was as mentioned earlier, because the setup that was used for studying the ±5°C resolution case was exactly the same as that of ±10°C resolution.

Figure 5-4 and Table. 5-2 refer to ±5ºC resolution tests. These tests were conducted between 270ºC and 300ºC, with increments of 5ºC. It was found that the percentage range of uncertainty as determined from the comparison of the experimental and theoretical graphs was found to be 0.70%. This is expected from the very fact that as the temperature resolution increases, the range of uncertainty in accurately determining the group velocity using experimentally determined values also increases.

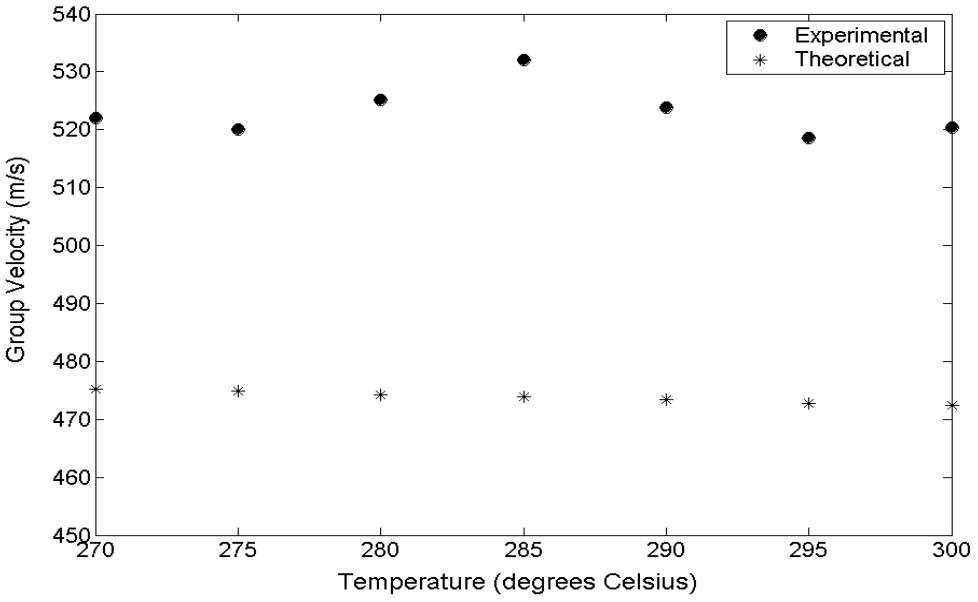

(a)

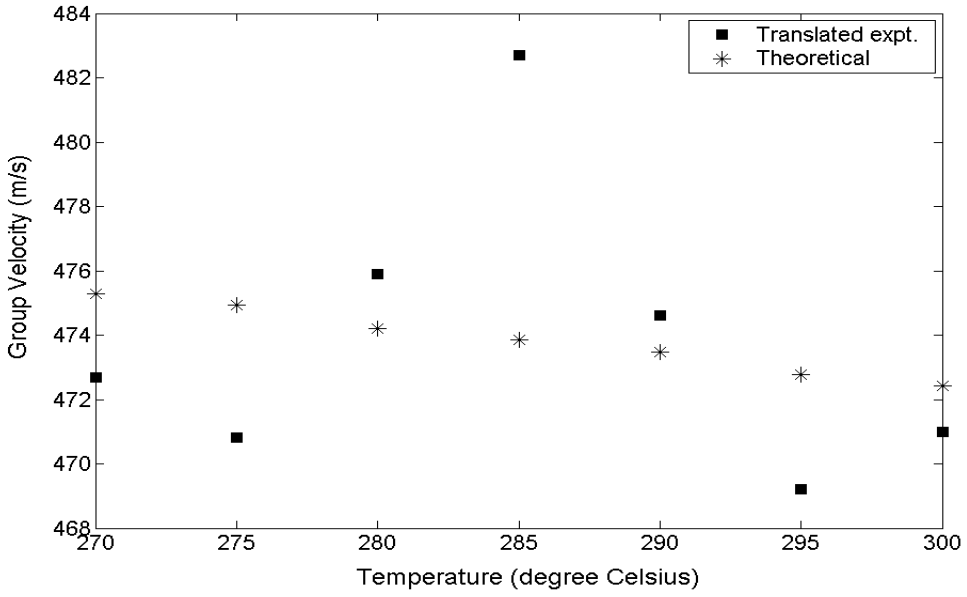

(b)

Figure 5-4 (a) Experimental versus theoretical group velocity for 23 KHz frequency for the ±5°C resolution, and (b) translated experimental group velocity as compared to theoretical group velocity

Table 5-2 Group velocity translation and range of uncertainty calculation for ±5ºC resolution of the 23 KHz components

Temp (°C)	Expt. Group Velocity (m/s)	Theo. Group Velocity (m/s)	$GV_e - GV_{th}$ (m/s)	Average Diff (m/s)	New Expt. Group Velocity (m/s)	Range of Uncertainty	Percent
270	522	475.28	46.72	49.3	472.7	-0.005428379	0.543
275	520.12	474.92	45.2	49.3	470.82	-0.008633033	0.863
280	525.2	474.2	51	49.3	475.9	0.003584985	0.358
285	532	473.85	58.15	49.3	482.7	0.018676796	1.868
290	523.9	473.48	50.42	49.3	474.6	0.002365464	0.236
295	518.5	472.77	45.73	49.3	469.2	-0.007551241	0.755
300	520.3	472.42	47.88	49.3	471	-0.0030058	0.300

It is thus seen that, with the requirement of increased resolution, there occurs a simultaneous increase in the range of uncertainty. Depending upon commercial tolerance levels and requirements, the limits of TAP-NDE can be fixed to suit the needs of the industry.

THICKNESS DIFFERENTIATION RESULTS

Figure 5-5 shows the group velocity distributions obtained from the data analysis of the three types of wafers. On translating the data to the theoretical curve, it is seen that there is a high degree of correlation between the experimental and theoretical curves, and that TAP-NDE is able to distinguish between the three different types of wafers, by picking a frequency component for analysis, and studying its group velocity pattern with increasing temperature.

It is thus established that TAP-NDE is capable of resolving thickness and temperature simultaneously, by taking known values of thickness, and studying as to how group velocity is influenced for a particular frequency component.

The above tests were conducted up to 600ºC, and hence, it is possible to state that such a differentiation can be done until that temperature region. Also, these tests were conducted for known thickness values. In the industrial scenario, the thickness during in-situ processing would continuously change, because of which, the analysis of one single frequency component would prove to be insufficient to characterize temperature and thickness simultaneously.

In order to carry out simultaneous characterization of unknown thickness and temperature values, it becomes important to locate the frequency components that are sensitive to temperature and thickness separately, and to analyze them as demonstrated here. The above experimentation thus also lays a foundation as to the guidelines of analysis for different thickness measurements.

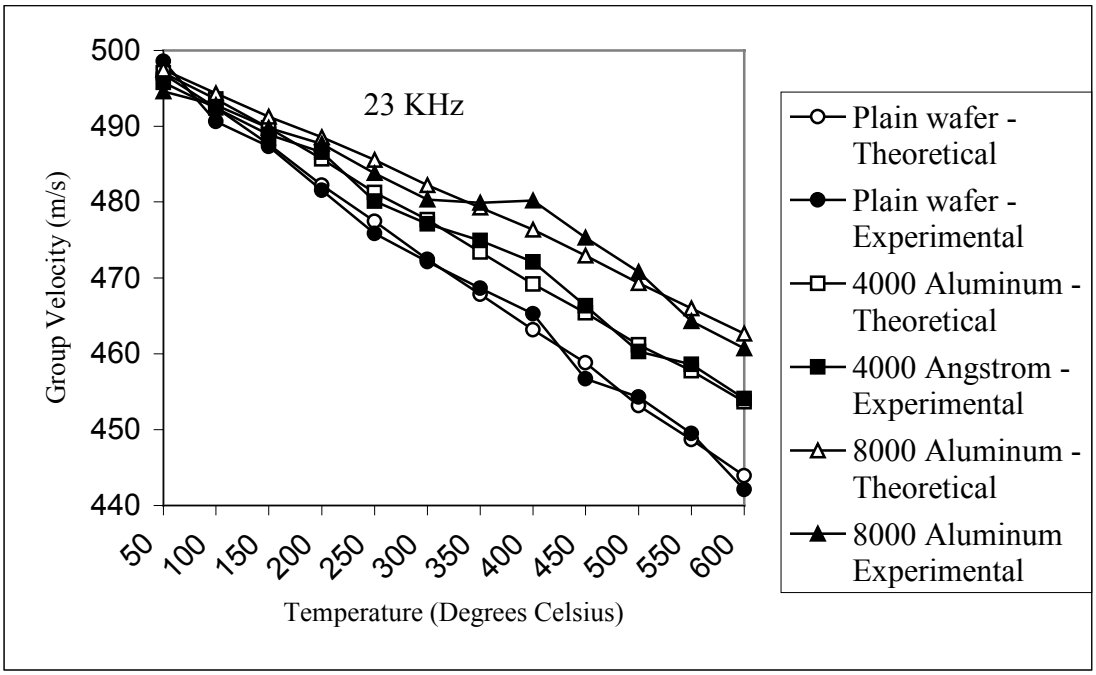

Figure 5-5 Plot showing group velocity variation for different thickness (indicated in the legend), as temperature increases from room temperature to 600°C.

CHAPTER VI

CONCLUSIONS

The need for a tool for in-situ characterization is becoming an increasingly important consideration in the industry, owing to increasing IC chip accuracy demands [21], and the impetus of technology towards nano scale operations. Existing methodologies are limited in their application towards the needs of tomorrow. Their output moves towards inadequacy, as the accuracy and tolerance levels required by the end users of IC chips increase.

TAP-NDE has been presented here as a suitable technique that can be a possible alternative to the existing need for simultaneous thickness and temperature characterization during wafer processing. Pyrometric techniques can answer for temperature determination alone, with certain accuracy, while thickness characterization requires specialized devices that have to be simultaneously implemented. Issues of in-situ performance of both these techniques are also to be accounted for, and a correlation between thickness and temperature has to be derived for such a setup.

The study in this thesis volume has helped in addressing the outlined objectives by theoretically and experimentally establishing the following:

- A theoretical model for obtaining the dispersion curves for different temperatures was obtained, which helped to identify the frequency components that were later on used for experimental analysis. This modeling was done using five elastic constants, which had to be included because of different crystal lattice structures for considering deposition layer effects.
- A theoretical model was developed to understand the change in the dispersion model for wafers of different thickness at different temperatures. The study was performed for

4000Å and for 8000 Å Aluminum as the deposition layers, with Titanium (250Å thickness) as the bonding layer.

- The theoretical models showing simultaneous temperature and thickness characterization were developed accordingly.
- The current study experimentally demonstrates the feasibility of TAP-NDE as a tool that can achieve an accuracy of up to ±5ºC in terms of temperature resolution at a temperature of up to 300ºC. The range of uncertainty for ±10ºC resolution was found to be 0.43%, while that of ±5ºC resolution was found to increase to 0.70%. Thus, there was an increase in uncertainty with increased requirement of resolution.
- The uncertainty that was observed in determining the group velocity was accounted for because of various reasons including spot size, read-off inaccuracy, and parallax error during determination of distance of flight of the wave.
- The study also demonstrates the ability to recognize the thickness of the grown wafer. This was achieved using single frequency component experimentally, as the thickness was known. For unknown thickness, it one must analyze at least two different frequency components to demonstrate this effect.

Temperature characterization is fairly easier because of the linear change of temperature with frequency for a constant wave number [22]. It is however, necessary to understand the change in thickness with frequency for a constant wave number, in order to identify and examine a particular frequency component for thickness characterization.

Identification of the most sensitive frequency band is crucial in terms of resolution [23,24]. At lower frequencies, thickness resolution is high, but it becomes difficult to achieve temperature resolution for wafers with deposition layers on it. Similarly, at higher frequencies, temperature resolution is pronounced, but thickness resolution becomes the impeding factor.

The solutions to the A_o mode have been presented here. Identification of higher anti-symmetric modes, and a study of symmetric modes is yet another improvement that can add to the viability of TAP-NDE. It can be seen on the theoretical curves that at higher modes, it becomes easier to achieve temperature resolution. However, with the existing technique, the excitation of a mechanical wave will consistently cause the creation of the A_o mode, and rarely create any other propagating modes. This is because, for the wavelength that is being generated, only the A_o mode is found to propagate. The ease of generating lower frequencies by imparting lower energy is also another reason for choosing the low frequency region as the belt for examination.

Laboratory conditions limit the capability of a high-temperature demonstration of TAP-NDE. However, as seen in the study, the problem of resolution occurs at lower temperatures, and not at higher temperatures. The group velocity curves for different thickness diverge at higher temperatures, which makes the issue of resolution only that much easier to deal with.

The pulsing laser can be adapted to the chamber system in the industry upon identification of the right excitation frequency. Such a study will help in switching from broadband to narrowband generation. As explained by Vandervort [25], the excitation laser beam can be reconfigured through a binary optical element to convert a single beam into a number of beams that are spatially and energetically similar diverging at a constant beam to beam angle.

Also, the access to the wafer can be taken care of by making generation a fiber-based technique. As described by Burger et al [17], the generation can occur through a bundle of fibers that would ultimately cause wave propagation. Simultaneously, the input energy for the system can be controlled by spot size, and thus, the precise spot-size can also be determined for the intended application. Care should however be taken to ensure that there is no ablation of wafer

surface during pulsing, which would otherwise create non-linear wave propagation, and result in wrong data, and wafer damage.

The wave detection system used in this study consisted of a dual FTI system, with each FTI receiving its coherent beam of light from a separate He-Ne laser. Multi-channel FTI systems can help achieve a better and a more complete study of the wafer, if they are distributed all along the radius of the wafer. The wafer, as it spins about its axis, can be studied at different points on its surface by timing the wave generation and sensing correspondingly, using a microcontroller mechanism. A direct digital hardware implementation of such a setup would create a complete wafer profile.

The GRIN lenses at the ends of the FTI are known to perform adequately well at temperatures of up to 250°C. They cannot be situated inside the thermal chamber, for want of temperature withstanding limitations. However, with higher laser power, their basic property of variable standoff distances can be exploited, by positioning them outside the chamber, and yet achieving the wave detection system.

The issue of the shift of experimental group velocity from theoretical group velocity, as seen in the experiment, is the result of inadequate FTI positioning and measurement systems under laboratory conditions. The determination of the exact location of the FTI beam is very crucial because of the small degree of changes in group velocity. Ideal positioning systems should house the GRIN lens perfectly perpendicular to the wafer on a continuous basis, without the requirement of minor adjustments to account for sending the returning beam of light from the wafer surface. This would also solve the issue of angular misalignments that possibly occurred during laboratory evaluation.

The use of better signal processing techniques is yet another issue with scopes of improvements. It is seen that the Gabor wavelet is adequately adaptive and sensitive to the

experimentally demonstrated resolution in terms of temperature and thickness. At the same time, this joint time-frequency processing technique is the reason for the limitation posed on resolution. The use of empirical mode decomposition (EMD) techniques, and Hilbert Transforms can help in better spatial and temporal localization, which would identify group velocities to a higher degree of accuracy. Such a tool would help in answering the issue of temperature and thickness resolution.

It is thus seen that there are various directions of improving TAP-NDE towards better industrial performance. Dedicated studies towards each of these identified issues relating to the overall system output needs to be dealt with before commercial materialization of the technique. However, this study was able to demonstrate the feasibility of this technique towards simultaneous thickness and temperature characterization during wafer processing. Upon removing all these obstacles that are basically design issues in the industrial implementation of TAP-NDE, it would be possible to minimize error and uncertainty, and edge towards greater accuracy and preciseness in solutions, which is what nano scale operations is all about. Each step in accuracy is a move towards a better solution for the unanswered problems in the industry.

REFERENCES

1 http://www.nobel.se/physics/educational/integrated_circuit/history/ (1995) Accessed on March 06, 2003.

2 D. Hodul, S. Metha, The use of semiconductor processes for the design and characterization of a rapid thermal processor, Nuclear Instruments and Methods in Physics Research 37/38 (1989) 818-822.

3 L. Asinovsky, L.E. Frisa, Control of PVD TiN thickness measurements, Microelectronic Engineering 37/38 (1997) 427-432.

4 J.P. Zollner, V. Cimalla, J. Pezoldt, RTP – Temperature monitoring by means of oxidation, Journal of Non-crystalline Solids 187 (1995) 23-28.

5 D.A. Hutchins, F. Nadeau, Non-contact ultrasonic waveforms in metals using laser generation and interferometric detection, Proceedings of the 1983 Ultrasonics Symposium (1983) 1175-1177.

6 R.J. Dewhurst, C.E. Edwards, A.D.W. Mckie, S.B. Palmer, Comparative study of wide-band ultrasonic transducers, Ultrasonics 25 (1987) 315-321.

7 K. Kishimoto, H. Inoue, M. Hamada, T. Shibuya, Time-frequency analysis of dispersive waves by means of wavelet transform, Transactions of the ASME Journal of Applied Mechanics 62 (1995) 841-846.

8 Y. Hayashi, S. Ogawa, H. Cho, M. Takemoto, Non-contact estimation of thickness and elastic properties of metallic foils by the wavelet transform of laser-generated Lamb waves, NDT&E International 32 (1999) 21-27.

9 D.C. Hurley, A.J. Richards, Thin-films elastic-property measurements with laser-ultrasonic SAW spectrometry, Thin Solid Films 398-399 (2001) 326-330.

10 M. Grimsditch, Effective elastic constants of superlattices, Physical Review B 31 10 (1985) 6818-6819.

11 C.C. Habeger, R.W. Mann, G.A. Baum, Ultrasonic plate waves in paper, Ultrasonics 17 2 (1979) 57-62.

12 D. Schneider, B. Schultrich, H.J. Scheibe, H. Ziegele, M. Griepentrog, A laser-acoustic method for testing and classifying hard surface layers, Thin Solid Films 332 (1998) 157-163.

13 G.A. Rabroker, Laser induced stress wave thermometry applied to silicon wafer processing, Masters Thesis, Texas A&M University, May 2000.

14 G. Simmons, H. Wang, Single Crystal Elastic Constants and Calculated Aggregate Properties: A Handbook, The M.I.T Press, Cambridge, England, 1971.

15 R.M. White, Generation of elastic waves by transient surface heating, J Appl Phys 34 12 (1963) 3559 – 3567.

16 J.D. Aussel, A. Le Brun, J.C. Baboux, Generating acoustic waves by laser: theoretical and experimental study of the emission source, Ultrasonics 26 (1988) 245 – 255.

17 C.P. Burger, N.A. Schumacher, C.E. Duffer, T.D. Knab, Fiber-optics techniques for generating and detecting ultrasonic waves for quantitative NDE, Optics and Lasers in Engineering 19 (1993) 121-140.

18 C.S. Suh, G.A. Rabroker, R. Chona, C.P. Burger, Thermal-acousto-photonics for non-contact temperature measurement in silicon wafer processing, Proceedings of SPIE 3783 (1999) 184-193.

19 V. Trivedi, S.J. Pearton, Evaluation of rapid thermal processing systems for use in CMOS fabrication, Solid State Electronics 46 (2002) 777-783.

20 C.K. Chui, An Introduction to Wavelets, Academic Press, San Diego, CA, 1992.

21 S.A. Campbell, The Science and Engineering of Microelectronic Fabrication, Oxford University Press, New York, 1996.

22 I.A. Viktorov, Rayleigh and Lamb Waves - Physical Theory and Applications, Plenum Press, New York, 1967.

23 H. Jeong, Analysis of plate wave propagation in anisotropic laminates using a wavelet transform, NDT&E International 34 (2001) 185-190.

24 H.C. Park, D.S. Kim, Evaluation of the dispersive phase and group velocities using harmonic wavelet transform, NDT&E International 34 (2001) 457-467.

25 K.D. Vandervort, Wavelength re-inforced thermo-acousto-photonic NDE of an elastomer to steel adhesive bond, Masters Thesis, Texas A&M University, May 1997.

APPENDIX - A

DETERMINATION OF ELASTIC CONSTANTS – MATLAB CODE

```
%-----------------------------------------------------------------------------------------------
% The objective of this code is to obtain the final effective elastic constants of the entire
% wafer model.  The deposition layers are modeled first together, and then this new
% combined unit is again modeled similarly with the substrate.  The input parameters in
% each case would be the two different thickness involved, and the independent elastic
% constants of each of the layers.  Since this model incorporates changing temperature,
% the elastic constants for each temperature (in steps of 50°C) is given as input, from
% data books)
%-----------------------------------------------------------------------------------------------

n=12;
d1 = input('thickness of layer 1 (upper layer) : ');
d2 = input('thickness of layer 2 (lower layer) : ');

c111=[1.0567
      1.0394
      1.0195
      0.9983
      0.9772
       0.956
      0.9348
      0.9134
      0.8916
      0.8694
      0.8458
      0.8211];

% c111 – C11 elastic constant of layer 1 for different temperatures from 50°C to 600°C.

c131=[0.6012
      0.5971
       0.593
      0.5883
      0.5839
      0.5782
      0.5724
      0.5676
      0.5615
       0.556
      0.5494
      0.5427];

% c111 – C11 elastic constant of layer 1 for different temperatures from 50°C to 600°C.
```

```
%-------------------------------------------------------------------------------------------------
%  In a similar fashion, data for c331 and c551 (belonging to the first layer), and c112,
%  c132, c332, and c552 (belonging to the second layer) are included in the code.
%-------------------------------------------------------------------------------------------------


% CALCULATIONS FOR ALUMINUM AND TITANIUM COMBINATION– BASED %
UPON THE CHAPTER-2 MODEL FOR DEPOSITION LAYER EFFECTS

f1=d1/(d1+d2);                  % Fractional thickness of layer 1
f2=d2/(d1+d2);                  % Fractional thickness of layer 2

for k=1:n                       % Loop for determination of effective elastic constants

   C33(k) = 1./(f1./c331(k)+f2./c332(k));

   C13(k) = (f1.*c131(k).*c332(k) + f2.*c132(k).*c331(k))./(f1.*c332(k)+f2.*c331(k));

   C11(k) = f1.*c111(k) + f2.*c112(k) + f1*(c131(k)./c331(k)).*(C13(k)-c131(k)) +
            f2*(c132(k)./c332(k)).*(C13(k)-c132(k));

   C55(k) = 1./(f1./c551(k)+f2./c552(k));

end


%-------------------------------------------------------------------------------------------------
% CALCULATIONS FOR NEW COMBINED LAYER AND SILICON SUBSTRATE
% COMBINATION– BASED % UPON THE CHAPTER-2 MODEL FOR
% DEPOSITION LAYER EFFECTS


h1 = input('thickness of layer 1 (upper layer Al/Cu + Ti) : ');

h2 = 5250000;                           % Thickness of substrate

g1=h1/(h1+h2);                          % Fractional Thickness of layer 1 ( Al + Ti )
g2=h2/(h1+h2);                          % Fractional Thickness of layer 2 ( Silicon)

T(1)=50;                                % Temperature initialization

for t=1:n                               % Loop for elastic constants determination of Si

        csi11(t)=1.6578-0.00015570160*(T(t)-25);
        csi13(t)=0.6394-0.00006266120*(T(t)-25);
        csi33(t)=1.6578-0.00015570160*(T(t)-25);
        csi55(t)=0.7962-0.00006599330*(T(t)-25);
```

```
   T(t+1)=T(t)+50;
end

for k=1:n                                   % Final Effective Elastic Constants Loop

   c33(k) = 1./(g1./C33(k)+g2./csi33(k));

   c13(k) = (g1.*C13(k).*csi33(k) + g2.*csi13(k).*C33(k))./(g1.*csi33(k)+g2.*C33(k));

   c11(k) = g1.*C11(k) + g2.*csi11(k) + g1*(C13(k)./C33(k)).*(c13(k)-C13(k)) +
            g2*(csi13(k)./csi33(k)).*(c13(k)-csi13(k));

   c55(k) = 1./(g1./C55(k)+g2./csi55(k));

end
```

APPENDIX - B

WAVE DISPERSION EQUATION – FORTRAN CODE FOR SYMMETRIC AND ANTI-SYMMETRIC MODE GENERATION

```
**********************************************************************
* This code is used to obtain the different dispersion modes of the Lamb wave that has been
*initiated on the specimen.  The general equations for the orthotropic wave dispersion model
*have been adopted from the paper on Ultrasonic waves in Paper by Habeger et al.  The
*different symmetric and anti-symmetric modes are plotted as functions of wave number versus
*frequency.
**********************************************************************
implicit none

      real(8) w,freq,kx,ReKzsqp,ReKzsqm,ReRatio,IeRatio,r
      complex(8) B,D,kzsqp,kzsqm,kzp,kzm,rp,rm,gp,gm,hp,hm,E
      complex(8) c11,c13,c33,c55,p,l,RElast,IElast
      complex(8) i
      real(8) RE,IE,aRE,aIE,epsilon,T

      open(8,file='m:\datsubst.dat')

      i=(0, 1)
      r=0
      freq=0
      kx=0
      RElast=1
      IElast=1
      epsilon=1
      T=25

      c11=(16.578*10**10)-1.576*10**7*(T-25)
      c13=6.394*10**10-6.368*10**6*(T-25)
      c33=16.578*10**10-6.669*10**6*(T-25)
      c55=7.962*10**10

      p=2331.0                                  * Density
      l=0.0002625                               * thickness

do while(freq.le.3000000)                       * Frequency loop

      kx=0
      w=freq*2*3.1415
      do while(kx.le.7000)                      * Wave number loop


      B=p*(c33*((c11/p)-((w**2)/kx**2))-c13*(2*c55+c13)/p-c55*(w**2)
     c            /(kx**2))/(c33*c55)
```

```
      D=(p**2)*((w**2)/(kx**2)-c55/p)*((w**2)/(kx**2)-c11/p)/(c33*c55)

      kzsqp=(kx**2)*(-B+sqrt((B**2)-4*D))/2
      kzsqm=(kx**2)*(-B-sqrt((B**2)-4*D))/2
      ReKzsqp=real(kzsqp)
      ReKzsqm=real(kzsqm)
      kzp=sqrt(kzsqp)
      kzm=sqrt(kzsqm)
      rp=(p*(w**2)-c11*(kx**2)-c55*kzsqp)/((c55+c13)*kx*kzp)
      rm=(p*(w**2)-c11*(kx**2)-c55*kzsqm)/((c55+c13)*kx*kzm)
      gp=c11*kzp*rp+c13*kx
      gm=c11*kzm*rm+c13*kx
      hp=kzp+kx*rp
      hm=kzm+kx*rm
      E=((exp(i*kzp*l)-exp(-i*kzp*l))/(exp(i*kzp*l)+exp(-i*kzp*l)))*
c           (hp*gm)-
c            ((exp(i*kzm*l)-exp(-i*kzm*l))/(exp(i*kzm*l)+exp(-i*kzm*l)))*
c           (hm*gp)
      RE=real(E)
      IE=imag(E)
      ReRatio=RE/RElast
      IeRatio=IE/IElast
      RElast=RE
      IElast=IE
      aRE=abs(RE)
      aIE=abs(IE)

      if(kx.ge.20)then


            if((aRE.le.epsilon).and.(aIE.le.epsilon))then
            if(r.eq.0)then
            write(*,*)kx,' ',freq
            write(8,*)kx,' ',freq
            r=1
            end if
            end if

            if((ReRatio.le.0).and.(aIE.le.epsilon))then
            if(r.eq.0)then
            write(*,*)kx,' ',freq
            write(8,*)kx,' ',freq
            r=1
            end if
            end if

            if((IeRatio.le.0).and.(aRE.le.epsilon))then
            if(r.eq.0)then
```

```
                r=1
                write(*,*)kx,' ',freq
                write(8,*)kx,' ',freq
                end if
                end if


        r=0

end if

        kx=kx+1
        end do

        freq=freq+1000
        end do

end
```

APPENDIX - C

GROUP VELOCITY CURVES – FORTRAN CODE

```
**********************************************************************
* This code determines the group velocity of each specified frequency band as against
* different temperatures.  Thickness is a variable, and hence, for different thickness, the group
* velocity distribution can be obtained.  This code can be adapted towards the A_o or the S_o
*modes.
* note: hm*gp in first term for antisymmetric modes
**********************************************************************
    implicit none

          real(8) w,freq,kx,ReKzsqp,ReKzsqm,ReRatio,IeRatio,r,bound
          complex(8) B,D,kzsqp,kzsqm,kzp,kzm,rp,rm,gp,gm,hp,hm,E
          complex(8) c11,c13,c33,c55,p,l,RElast,IElast
          complex(8) i
          real(8) RE,IE,aRE,aIE,epsilon,df,kxl,kxu,fl,fu,vg,T,ku,kl
    open(8,file='m:\tgv8023.dat')

          i=(0,1)
          r=0
          RElast=1
          IElast=1
          epsilon=10
          p=2331.7                    * density
          l=0.00026291                *  thickness
          T=50                        *  Initial temperature

**********************************************************************
* The desired frequency band, and the corresponding location of wave number band have to be
*specified below.  The wave number should be defined such that the code would cross only one
* mode (as can be located from the dispersion curves model – APPENDIX B)
**********************************************************************

          freq=23000
          df=250
          kxl=450
          kxu=750
          bound=kxl+1
          fl=freq-df
          fu=freq+df

**********************************************************************

do while(T.le.600)
          c11=16.608*10**10-1.5614*10**7*T
          c13=6.409*10**10-6.2818*10**6*T
```

```
      c33=16.604*10**10-1.5706*10**7*T
      c55=7.958*10**10-6.8198*10**6*T

      freq=fl
      do while(freq.le.fu)
            write(*,*)freq
            w=freq*2*3.141592654
            kx=kxl

      do while(kx.le.kxu)


      B=p*(c33*((c11/p)-((w**2)/kx**2))-c13*(2*c55+c13)/p-c55*(w**2)
c          /(kx**2))/(c33*c55)
      D=(p**2)*((w**2)/(kx**2)-c55/p)*((w**2)/(kx**2)-c11/p)/(c33*c55)
      kzsqp=(kx**2)*(-B+sqrt((B**2)-4*D))/2
      kzsqm=(kx**2)*(-B-sqrt((B**2)-4*D))/2
      ReKzsqp=real(kzsqp)
      ReKzsqm=real(kzsqm)
      kzp=sqrt(kzsqp)
      kzm=sqrt(kzsqm)
      rp=(p*(w**2)-c11*(kx**2)-c55*kzsqp)/((c55+c13)*kx*kzp)
      rm=(p*(w**2)-c11*(kx**2)-c55*kzsqm)/((c55+c13)*kx*kzm)
      gp=c11*kzp*rp+c13*kx
      gm=c11*kzm*rm+c13*kx
      hp=kzp+kx*rp
      hm=kzm+kx*rm
      E=((exp(i*kzp*l)-exp(-i*kzp*l))/(exp(i*kzp*l)+exp(-i*kzp*l)))*
c         (hm*gp)-
c         ((exp(i*kzm*l)-exp(-i*kzm*l))/(exp(i*kzm*l)+exp(-i*kzm*l)))*
c         (hp*gm)
      RE=real(E)
      IE=imag(E)
      ReRatio=RE/RElast
      IeRatio=IE/IElast
      RElast=RE
      IElast=IE
      aRE=abs(RE)
      aIE=abs(IE)

      if(kx.ge.bound)then
      if(freq.eq.fl)then
            if((aRE.le.epsilon).and.(aIE.le.epsilon))then
            kl=kx
            write(*,*)kl
            r=1
            kx=kxu
            end if
```

```
                    if((ReRatio.le.0).and.(aIE.le.epsilon))then
                    if(r.eq.0)then
                    kl=kx
                    write(*,*)kl
                    r=1
                    kx=kxu
                    end if
                    end if

                    if((IeRatio.le.0).and.(aRE.le.epsilon))then
                    if(r.eq.0)then
                    kl=kx
                    write(*,*)kl
                    r=1
                    kx=kxu
                    end if
                    end if

end if

        if(freq.eq.fu)then
                    if((aRE.le.epsilon).and.(aIE.le.epsilon))then
                    ku=kx
                    write(*,*)ku
                    r=1
                    kx=kxu
                    end if

                    if((ReRatio.le.0).and.(aIE.le.epsilon))then
                    if(r.eq.0)then
                    ku=kx
                    write(*,*)ku
                    r=1
                    kx=kxu
                    end if
                    end if

                    if((IeRatio.le.0).and.(aRE.le.epsilon))then
                    if(r.eq.0)then
                    ku=kx
                    write(*,*)ku
                    r=1
                    kx=kxu
                    end if
                    end if

        end if
```

```
        r=0
end if
        kx=kx+0.005

end do

freq=freq+2*df

end do

vg=(2*df*2*3.141592654)/(ku-kl)
        write(*,*)ku,' ',kl
write(*,*)T,' ',vg
        write(8,*)T,' ',vg
T=T+50

        end do

end
```

APPENDIX - D

GABOR WAVELET TRANSFORM – MATLAB CODE

```
%-----------------------------------------------------------------------------------------------
% The Gabor wavelet is used as the analyzing function for the experimentally obtained
% waveform.  This code is used to determine the time-frequency plot and the group
%  velocity plot from the input time-amplitude information
%-----------------------------------------------------------------------------------------------

load FTI1.txt;                    % input the experimentally obtained waveform data
x=FTI1;
T=x(:,1);
A=x(:,2);
len= length(x);

%-----------------------------------------------------------------------------------------------

N=len;

dt=T(3)-T(2);

sampfr=1/dt;                                        % sampling frequency (Hz)
maxfr=sampfr/2;

userfr=input('Enter required maximum frequency on y-axis (in Hz) = ');

if userfr>maxfr
   disp(‘Reduce your maximum frequency');
else
   disp('Maximum Frequency is within limits');
end

timestep=input('Enter number of time steps : ');
scalestep=input('Enter number of frequency steps : ');

Gam=input('Enter gamma value : ');                  % Gamma value

dist1=input('Enter distance of FTI from generation : ');

M=ceil(userfr*N/maxfr);

timeinc=(T(N)-T(1))/timestep;
scaleinc=userfr/scalestep;

u=[T(1):timeinc:T(N)];
W=[0:scaleinc:userfr/2];
```

```
a=1./W;                                          % Scaling parameter

d1=0;
for p=0:(N/timestep):N                           % Time loop

   d1
   d1=d1+1;
   c2=0;

   for q=0:(N/scalestep):ceil((N+1)/2)           % Frequency loop
         c2=c2+1;

          y(c2,d1)=sum((1./sqrt(a(c2))).*(1/(pi)^0.25).*sqrt(2*pi/Gam).*((A)').*exp(-
          (0.5*((2*pi/Gam).*(((0:N-1)-p)./a(c2)).*dt).^2)).*cos(2*pi*((((0:N-1)-p)./a(c2)).*dt)));
   end

   Mag=abs(y);

end

figure;
grid on;
contour3(u,W,Mag);
view(2);
shading interp;
axis tight

xlabel('Time (seconds)');
ylabel('Frequency (Hz)');
title('GABOR WAVELET TRANSFORM (FTI-1)');

%-----------------------------------------------------------------------------------------------------
% The portion of the code below is used to determine the extrema of the frequency
% coefficients in each row of the wavelet magnitude matrix, and then calculate the group
% velocity using the distance from the point of generation
%-----------------------------------------------------------------------------------------------------

N=(scalestep/2)+1;
D=zeros(size(Mag));
times=zeros(N);
for g=1:N
   B=Mag(g,:);
   [C(g),i(g)]=max(B);
   ti(g)=u(i(g));
   for k=1:N
      if k==i(g)
         times(g)=[u(g)];
      end
```

```
   end
end
time=zeros(size(Mag));
for t=1:N
   for s=1:N
      if s==i(t)
         D(t,s)=[C(t)];
         time(t,s)=[u(t)];
      end
   end
end

gvel=(dist1*0.001)./ti;
figure; plot(gvel,W,'*')
title('GROUP VELOCITY PLOT (FTI -1)')
xlabel('Time (seconds)');
ylabel('Frequency (Hz)');
axis([200 1000 0 10e4]);
```

VITA

Vikram Vedantham was born in Chennai, a city in the south of India, on March 03, 1979. After graduating from high school in Chennai, he enrolled at Annamalai University, Chidambaram, India, for his undergraduate studies in mechanical engineering. He obtained his B.E in mechanical Engineering in May 2000, specializing in design and mechanics. After graduation, he joined Texas A&M University in August 2000, pursuing his Masters degree in mechanical engineering. He started working for Dr. Chii-Der S. Suh as a graduate research assistant in August 2001, working on the use of Photo-mechanics for Non-Destructive Testing. During his graduate studies, he worked on employing TAP-NDE for examining various specimens such as composites, railroad tracks and semiconductor wafers. Based on his research work, he has published papers at ASNT, ASME and SEM conferences. Mr. Vedantham's permanent mailing address is Vikram Vedantham, Flat No. 2, New no. 8, Rukmani Street, West Mambalam, Chennai 600 033, Tamil Nadu, India.